Universidad de La Laguna
Faculty of Science, Physics Section

Master Degree in Astrophysics
Final Master Project

The Fate of Accreted Stars in the Milky Way

Supervised by:
Dr. Chris Brook
Dr. Robert Grand

Author:
Guacimara García Bethencourt

Academic year 2021/2022
San Cristóbal de La Laguna - July 2022

Table of Contents

Resumen

Las simulaciones cosmológicas basadas en el modelo ΛCDM sugieren que la formación y evolución de las galaxias viene dada a través de la unión jerárquica de pequeñas estructuras. Datos obtenidos mediante observaciones, conjuntamente con el uso de simulaciones numéricas, han proporcionado información sobre algunas estructuras estelares originadas en galaxias satélite, que se han fusionado con la Vía Láctea en el pasado. Algunas de las estructuras más importantes son aquellas conocidas como *Gaia-Enceladus*, las corrientes de Helmi, o la galaxia enana de Sagitario. Estos *mergers* (galaxias satélite que se han fusionado con la galaxia central) no solo forman parte de la propia Vía Láctea, sino que además han podido tener cierto impacto sobre ella durante su caída en el pozo de potencial del sistema. Por tanto, los procesos de acreción de galaxias satélite dejan ciertas pistas que pueden ser estudiadas por medio de la cinemática de las estrellas, ya que estas aún conservan algunas propiedades en la actualidad y presentan correlaciones en el espacio de fases. Esto permite identificar dichas estructuras dentro de nuestra galaxia, así como obtener detalles de su pasado de formación.

En este Trabajo de Fin de Máster, se ha utilizado una simulación de una galaxia análoga a la Vía Láctea para estudiar su historia de formación y caracterizar una serie de galaxias satélite que han pasado a formar parte de este sistema. Nuestra galaxia simulada pertenece al programa MaGICC y al grupo de simulaciones de MUGS. Esta simulación es generada con el código `Gasoline`, basado en la dinámica de N cuerpos y la Hidrodinámica Suavizada de Partículas, que además incluye otros procesos a menor escala como el enfriamiento y difusión de metales, la formación estelar, y el feedback de estrellas y de supernovas. Para el análisis se ha empleado un paquete de Python denominado Pynbody, desarrollado especialmente para este tipo de simulaciones. La simulación de estudio cuenta con unos 8 millones de partículas de estrellas, gas y materia oscura. A un redshift de 0.02 la galaxia tiene una masa total de 150.82×10^{10} $M_\odot$ y un radio virial de 241.99 kpc. Este sistema es similar a la Vía Láctea en aspectos como su masa, morfología, composición química o historia de formación, entre otros.

Los objetivos de este trabajo son: estudiar la cinemática y el espacio de fases de una serie de *mergers*, y comparar entre los más tempranos y los más tardíos; caracterizar algunas de sus propiedades antes de su acreción en la galaxia; estudiar el efecto de la colisión de una estructura análoga a *Gaia-Enceladus*; y analizar la contribución de estrellas formadas *ex-situ* a la región del bulbo galáctico. Para ello, se selecciona una serie de galaxias satélite de la simulación en el momento anterior a su acreción, de manera que se definen según su contenido en estrellas, gas y materia oscura en dicho paso temporal. Estos sistemas han sido previamente rastreados hasta ese momento desde épocas más tempranas por medio de una estrella guía situada en el centro de cada uno de ellos, que se utiliza como referencia para identificar cada galaxia satélite en cualquier captura temporal (*snapshot*) y definir así, su redshift o tiempo de caída en el sistema central.

Se han representado y analizado las distribuciones estelares de cada uno de los *mergers* en el espacio de fases para diferentes corrimientos al rojo (*redshifts*) después de su acreción. Se escogen los espacios definidos por las componentes de velocidad, la energía total y la componente vertical del momento angular. Los resultados de este análisis indican que las estructuras procedentes de galaxias satélite que se incorporan antes al sistema central muestran movimientos más aleatorios, están más mezclados en el espacio de fases, y se encuentran a bajas energías actualmente. Por el

contrario, aquellos *mergers* más tardíos presentan una rotación predominante (a veces retrógrada), conservan gran parte de su estructura inicial en el espacio de fases, y se localizan a altas energías, estando débilmente ligados al sistema. Por otro lado, se encuentra que la estructura similar a *Gaia-Enceladus*, en su unión a la galaxia, tiende a aumentar la dispersión de la componente vertical de velocidad de las estrellas pertenecientes a anteriores *mergers*. Este resultado es análogo al "calentamiento" del disco grueso primordial de la Vía Láctea debido a la estructura real de *Gaia-Enceladus*. Asimismo, es nuestra simulación este cuerpo es el que más contribuye al bulbo estelar de todas las estructuras estudiadas, aunque solo una pequeña parte de sus estrellas se localizan en esa región. Además, se tiene que aquellas estrellas absorbidas más temprano por la galaxia se concentran en las regiones más centrales (pero contribuyen más a la parte externa del bulbo), mientras que los *mergers* más tardíos se localizan fuera de este y están más dispersos en el halo estelar. Para el conjunto de todas las estrellas *ex-situ*, se tiene que: 1) más del 70% se sitúan en las regiones exteriores al bulbo; 2) la gran mayoría de estrellas en el bulbo han nacido *in-situ*. Por último, las galaxias satélite más tempranas caen directamente al sistema principal y desde menores distancias, mientras que las posteriores provienen de mayores distancias y presentan varios pasajes apocéntricos y pericéntricos. Las primeras tienen historias de formación estelar más cortas y muestran aumentos en el ritmo de formación estelar antes de su acreción, probablemente debido a compresiones del gas durante este proceso. Los *mergers* tardíos presentan historias de formación estelar más extendidas en el tiempo, que decaen progresivamente. Los resultados sugieren que la población de estrellas *ex-situ* originada en galaxias satélite con tiempos de acreción menores, es más vieja en promedio que la de aquellos sistemas que caen más tarde en la galaxia principal.

Chapter 1

Introduction

The formation and evolution of galaxies within the Lambda Cold Dark Matter (ΛCDM; Frenk et al., 1985; Peebles, 1998) framework is given through a hierarchical merging of minor structures (Springel et al., 2005), leading to larger systems that continue to grow via gravity over time. Cosmological simulations of galaxies developed within this setting agree with the hierarchical formation of the Milky Way (MW) via mergers (e.g. Guo et al., 2011; Kormendy, 2013). These were initially more numerous due to the higher density of the Universe in its early stages (e.g. Abraham et al., 1996) that eased the gathering of matter to form plenty of small structures. As time went by, not only the main galaxy evolved, growing in size and changing in composition, but also its environment and minor companions, and the merger activity became less frequent.

The Milky Way is said to have gone through a variety of merger events that constitute its merger history. Observational data together with results from numerical simulations have offered important findings about past satellite galaxies that have being swallowed by our galaxy. These merger events have left behind stellar debris and structures within the MW, such as the well-known Gaia-Enceladus (GE) (Helmi et al., 2018) or Gaia Sausage (Belokurov et al., 2018). Other identified structures are those originated by: the Sagittarius (Sgr) dwarf galaxy (R. A. Ibata et al., 1994); Sequoia (Myeong et al., 2019); the Helmi Streams (Helmi et al., 1999); Thamnos (H. Koppelman et al., 2018); the proposed Kraken (Kruijssen et al., 2020); or the more recently discovered structure called Pontus (Malhan et al., 2022). These structures, although being more frequent at early times, can also take place nowadays. The Sgr dwarf galaxy, due to its orbit and late time of infall, has had a slow accretion process, leaving a disrupted stream of stars (R. Ibata et al., 2020; Vasiliev and Belokurov, 2020) that had its first passage into the Milky Way around 5.7 Grys ago (Ruiz-Lara et al., 2020), and is still being in torn apart. The ongoing interaction between the Milky Way and the Large Magellanic Cloud (LMC) is another example of a present/inminent merger event in our galaxy (Cautun et al., 2018).

In addition to becoming integrants of the Milky Way itself, these mergers could have also had a great impact on already formed stellar structures within the galaxy, i.e. previously accreted stars (or early ex-situ stars) or those born inside of the main galaxy (in-situ stars). The effects are more drastic especially for early massive mergers, as they collide with a partially formed and less massive galaxy at those times (i.e. larger mass ratio between mergers and the MW). Kinematically speaking, the stellar orbits of stars could have suffered variations due to these merger events. A particular good example is the impact that the Gaia-Enceladus-Sausage (GES) had on the primitive MW. This past dwarf satellite galaxy is thought to have "heated" a fraction

of the primordial thick disk after its accretion (e.g. Zolotov et al., 2009; Gallart et al., 2019), into a "hot thick disk" (Helmi et al., 2018; Di Matteo, P. et al., 2019) with halo-like kinematics known as the "splash" (Belokurov et al., 2020). On the other hand, accretion events could cause strong episodes of stellar formation (e.g. Brook et al., 2004; Grand, Bustamante, et al., 2017), as they inject new gas and dust in the galaxy. In this way, mergers are not only assembly pieces of the Milky Way, but also important external drivers of its growth and evolution.

Hence, mergers leave numerous hints of their accretion that can be studied to extract a better view of the merger history of the galaxy. This type of research is often carried out within the field of *Galactic Archaeology*, that is based on measuring features of stars in the present-day to obtain information about their orbits, chemical abundances, ages, etc., in order to unveil the formation scenario of our galaxy. Behind this idea, kinematical properties of stars play an essential key role on the quest for past merger events. When stars belonging to an outer minor system are attracted by a more massive galaxy, their trajectories tend to maintain a similar movement to the one the progenitor satellite had before starting to be tidally disrupted (Johnston et al., 1996; Johnston, 1998). This leads to correlations in phase space, where accreted systems conserve certain features during their consequent evolution inside the galaxy (Helmi and White, 1999). The different velocity components in the 3-dimensional space are able to describe the stellar orbits in terms of their orientation and account for the amount of rotation they have. Other variables, such as the orbit eccentricity, angular momentum or energy (these last two used to describe the Integrals of Motion (IoM; Helmi and Tim de Zeeuw, 2000)), are also important quantities to take into account in this field of investigation in an effort to unmask the origin of stars, the evolution of their orbits prior to the accretion, and posterior movement inside of the host galaxy.

All of this knowledge also needs to be considered to pin down the stars in the different galactic components (e.g. Bland-Hawthorn and Gerhard, 2016). For instance, orbits with random orientations and large velocity dispersion are associated to stars belonging to the bulge and stellar halo (i.e. pressure supported stellar structures), whilst orbits with a predominant orientation and small velocity dispersion are more likely to be part of the disk (i.e. rotationally supported stellar structures). It is suggested by several researches (e.g. Matsuno et al., 2019; Helmi, 2020) that the stellar halo of the galaxy is dominated by debris of accreted stars, thus, it inherits their kinematics. This debris can have long phase-mixing timescales, therefore its phase space coordinates/structures can remain distinct for long periods of time. On one hand, the inner halo is likely to be formed mainly via early massive mergers (Helmi et al., 2002; Cooper et al., 2010), since they fall from smaller distances and are closer to the potential well of the proto-galaxy in the moment of their accretion. On the other hand, in the outer halo late mergers seem to be the main stellar constituent (e.g. Belokurov et al., 2006; Bell et al., 2008; Helmi et al., 2011), due to their higher potential energy and larger infall distances. Besides, late mergers are more metal poor, older and less massive, hence, they have not suffered dynamical friction and sunk to the centre of the galaxy. On the contrary to accreted stars, in-situ stars prevail in the thin and thick disks, where molecular clouds of gas responsible for stellar formation are found. Hence, these stars reside in a different region of the velocity and Integrals of Motion spaces because of their disk-like kinematics.

There is a variety of astrometric and photometric missions like *Gaia* (Gaia Collaboration et al., 2018), and spectroscopic surveys like APOGEE (Majewski et al., 2017), GALAH (De Silva et al., 2015) or RAVE (Kunder et al., 2017), that have provided fundamental data to help

disentangle the merger history of the MW and determine the repercussions of these events. Along with observational results, many numerical simulations such as MaGICC (Brook et al., 2012; G. S. Stinson et al., 2012), AURIGA (Grand, Gómez, et al., 2017), EAGLE (Schaye et al., 2015; Crain et al., 2015), or NIHAO (Wang et al., 2015), developed to reproduce the formation and evolutionary processes of galaxies, are able to offer precise and reliable data capable of giving a more extended picture of the properties of the Milky Way and its past. The key of these simulations is their capacity to interpret the "fossil records" observed in the present day stellar distribution.

The present work approaches the study of the merger history of a simulated Milky Way from the MaGICC program through the characterisation of a set of mergers and the kinematical properties of ex-situ stars. The objectives of this project are described in the following chapter. In chapter 3, we provide the details of the simulation used in this study. Chapter 4 contains a guide on the methodology followed to carry out this analysis, starting from the characterisation of a selection of mergers. Next, we present the process to identify the mergers in each timestep of the simulation, and then, we give a brief basis on the kinematical magnitudes studied in this project. In section 5, they are exposed and discussed the outcomes of the kinematical evolution of accreted stars in velocity and IoM spaces from their time of infall to the present day. We lay special emphasis on the effects of a major merger event on the distributions of accreted stars and possible variations in their orbits. To accompany these results, we also explore the radial trajectories of the mergers before their accretion, their star formation history, and their final contribution to the stellar bulge, along with their density profile at redshift zero. In chapter 6, we conclude with a summary of the main results and implications of this work, and with a possible future perspective on research based on the same field of study. Lastly, it is presented in the appendix the routine selected to visualise mergers in phase space, based on a Kernel Density Estimation (KDE) plot, and its comparison to an ordinary 2-dimensional histogram.

Chapter 2

Objectives

This project aims to analyse the evolution of mergers from a simulated Milky Way analogue galaxy according to the velocity components, total energy and angular momentum of their constituent stars, from the moment they start becoming part of the main galaxy to the present day. We also intend to characterise these mergers and analyse how much they contribute to the inner regions of the galaxy. Particularly, the main objectives of this project can be itemised as follows:

- Analyse the merger history of a Milky Way-like galaxy and the evolution of ex-situ stars in velocity space and in Integrals of Motion space.
- Characterise the main properties of a sample of mergers before their accretion and at redshift zero.
- Compare the evolution and features between early mergers and late mergers.
- Study the possible impact of a major merger event, analogue to Gaia-Enceladus, on the orbits of other accreted structures.
- Analyse the contribution of accreted stars to the outer part of the galactic bulge at the present time.

Chapter 3

The Simulation

The simulated galaxy of analysis has been developed within the Making Galaxies in a Cosmological Context (MaGICC) project (G. S. Stinson et al., 2012; Brook et al., 2012). This program has a set of several cosmological hydrodynamical simulations of galaxies able to reproduce scaling relations from observations. The studied mock galaxy is also part of the McMaster Unbiased Galaxy Simulations[1] (MUGS; G. S. Stinson et al., 2010), which is a set of 16 high-resolution galaxy formation simulations of several different spiral and elliptical galaxies. In order to generate and evolve these simulations, it is used the particle based (Lagrangian) code known as `Gasoline`[2] (Wadsley et al., 2004), which accounts for the gravitational evolution of the collisionless particles (stars and dark matter) through N-body dynamics, and processes the fluid components (gas) via the usage of Smooth Particle Hydrodynamics (SPH; Gingold and Monaghan, 1977; Monaghan, 1992). On the other hand, to better reproduce the scenario of galaxy formation and evolution as a whole, `Gasoline` also implements numerous physical processes that are essential to handle small scale phenomena. These processes are referred to as sub-grid physics and the most important ones to consider are described in the next section.

The software that has been employed to read and analyse the simulation is a Python based package named Pynbody[3] (Pontzen et al., 2013), which has been specially developed for these type of simulations. On the other hand, the study has been accomplished within *LaPalma*, one of the 14 node facilities from the Red Española de Computación (RES), and located in the CALP (Centro de Astrofísica de La Palma).

3.1 Sub-grid physics

Sub-grid physic models in cosmological simulations deal with those mechanisms that are fundamental for galaxy formation to take place, but operate on smaller scales than the simulation's resolution itself. Despite of being beyond the resolution limit, these processes are of great impact to the large scale system, since they drive the evolution of its constituents. In the following subsections we briefly outline and describe the main processes to take into account for our particular simulation, namely: metal cooling and diffusion, star formation, and feedback from stars and supernovae.

[1] http://mugs.mcmaster.ca/description.html
[2] https://gasoline-code.com/
[3] https://pynbody.github.io/pynbody/

3.1.1 Metal Cooling and Diffusion

Cooling processes allow gas to lose enough energy and grow overdensities to set on star formation, which is more efficient for regions with higher metallicity. `Gasoline` includes gas cooling due to H, He, and several metal lines (Shen et al., 2010), implemented by the `CLOUDY` code (Ferland et al., 1998) and exposed to a UV ionising radiation background (Haardt and Madau, 1996). Along with this external UV radiation, it is applied Compton and radiative cooling acting as a feedback to provide photoionisation and heating to the Interstellar Medium (ISM). Besides, metal cooling depends on the diffusion of metals (e.g. C, O, Fe, Si, N, Mg), which is carried out through a turbulence mixing algorithm (Wadsley et al., 2008) and helps to enrich the galactic medium.

3.1.2 Star Formation

The formation of stars is a phenomenon that arises in a dense gaseous environment, usually enhanced with material from previous generations of stars. In aim to build the ideal scenario for this events to take place, high-density regions are created within the simulation and new stars are born when the gaseous mass of these areas overcome the Jeans mass. However, in order to resolve this specific mass and avoid the gravitational collapse of gas particles to smaller distances than the resolution limit of the simulation, it is applied a pressure field (Robertson and Kravtsov, 2008) in star forming regions. This is supplemented with a maximum threshold density, that is given according to the width of the SPH kernel (G. Stinson et al., 2006) and sets a minimum smoothing length of $\epsilon = 155$ pc. The latter value is $\frac{1}{4}$ times the gravitational softening length defined in the equations of motion.

Star formation sets on when gas reaches a temperature of $T < 10^4$ K and a density of $n_{th} > 9.3$ cm^{-3}. The amount of gas that is converted to stars is given by the Kennicutt-Schmidt law (Schmidt, 1959; Kennicutt, 1998):

$$\frac{\Delta M_\star}{\Delta t} = c_\star \frac{M_{gas}}{t_{dyn}} \tag{3.1.1}$$

where $\Delta M_\star$ is the mass of the stars formed, Δt is the timestep between the star formation events, $c_\star$ is the star formation efficiency, M_{gas} is the mass of the gas particles, and t_{dyn} is the dynamical or free-fall time, i.e. the time the gas requires to collapse to form stars. During the temporal interval defined by t_{dyn}, a fraction of gas given by $c_\star = 0.167$ is turned into stars. Equation 3.1.1 establishes a star formation rate proportional to $\rho_{gas}^{1.5}$ for MaGICC simulations, where ρ_{gas} is the gas density.

The individual stellar particles formed according to the Kennicutt-Schmidt law in this simulation are collisionless and represent clusters of co-eval stellar populations, i.e. each particle corresponds to a Single Stellar Population (SSP). To characterise the initial distribution of mass of these clusters, it is used the Chabrier (Chabrier, 2003) Initial Mass Function (IMF).

3.1.3 Stellar Feedback

Stars form and evolve and in turn, they feed the ISM with their energy. The stellar feedback considered in these simulations is implemented by using two different models. The first type of feedback, dubbed Early Stellar Feedback (ESF; G. S. Stinson et al., 2012), is related to the

energetic radiation ejected by young massive stars before they reach the supernova phase. This pre-SN feedback is injected into the ISM in the form of thermal radiation from UV photons and stellar winds that heat, photoionise and mix the surrounding gas and metals. Therefore, the ESF is also able to give pressure support from heated gas that halts its collapse and regulates star formation.

The second model of feedback owes to supernovae events, both to type Ia supernovae (SNIa; for binary systems with a white dwarf) and to type II supernovae (SNII; for massive stars) explosions. Massive stars (here, those more massive than 8 $M_\odot$) at the end of their lives explode into energetic bursts, generating a shock that rapidly expands through the medium. This is implemented via the blast-wave formalism (G. Stinson et al., 2006) to ensure that the energy is radiated away from the explosion in a reasonable timescale according to the temporal resolution limit of the simulation. In order to make this feedback effective, radiative cooling is turned off within the blast radius, so that dense regions of gas cannot be quickly radiated away. Analogously to the ESF, supernovae feedback also helps to regulate star formation by expanding and heating the ISM to prevent the collapse of gaseous clouds or by compressing certain regions to stimulate it. On the other hand, this process allows the input of elements formed inside the stars into the ISM, and give rise to the suitable conditions for heavy metals to be created, increasing the metallicity of the system.

3.2 Sample galaxy

The sample galaxy of this study is a zoom simulation of a late-type isolated galaxy tagged as `g15784` in the MUGS set. It constitutes a Milky Way-like galaxy, with a similar total mass to that of the real one. In fact, it is the closest analogue to our Milky Way out of all MaGICC galaxies (Gibson, B. K. et al., 2013; Walker et al., 2014; Brook et al., 2020), not only due to its mass and morphology, but also in terms of chemical composition, disk properties, and merger history.

3.2.1 Description

The simulation covers a time range starting with a Universe of $\sim$ 0.1 Gyr of age, to the present day, $\sim$ 13.8 Gyr after the Big Bang. However, we focus on the evolution given in the interval between 1.09 Gyr (z = 5.53) and 13.51 Gyr (z = 0.02). At z = 0.02, there are $\sim$8 million particles (stars, gas, and dark matter) residing in a box with 67 Mpc sides. At this redshift there are $\sim$4 million particles within a virial radius of 241.99 kpc, where the total, stellar and gaseous mass are $M_{total} = 150.82 \times 10^{10}$ $M_\odot$, $M_\star = 8.28 \times 10^{10}$ $M_\odot$, and $M_{gas} = 13.50 \times 10^{10}$ $M_\odot$, respectively. On the other hand, the average masses of the stellar, gas and dark matter particles within the simulation are 3.85×10^4 $M_\odot$, 2.05×10^5 $M_\odot$, and 1.11×10^6 $M_\odot$, respectively.

3.2.2 Cosmological Initial Conditions

The cosmological parameters of this simulations agree with the values obtained from the Wilkinson Microwave Anisotropy Probe Three (WMAP3; Spergel et al., 2007) observations of the Cosmic Microwave Background (CMB; Penzias and Wilson, 1965). Therefore, we have the following values: $H_0 = 73$ km s^{-1} Mpc^{-1} for the Hubble constant, $\Omega_m = 0.24$ for the mass density of the Universe, $\Omega_\Lambda = 0.76$ for the density associated to the cosmological constant, $\Omega_b = 0.04$

for the density associated to the baryonic mass, and $\sigma_8 = 0.79$ for the amplitude of density fluctuations. Although WMAP3 results are slightly different from Planck's (Planck Collaboration et al., 2020), this has no effect on the analysis of this project because it approaches the merger history of a single galaxy that is possible in both cosmological models. Nonetheless, the difference between the two cosmologies (WMAP3's and Planck's) arises in studies with large populations of galaxies, where results are statistically significant.

3.2.3 Merger history

The simulated galaxy of analysis has a particular merger history that holds great similarity with the formation path of the Milky Way. There is high merger activity at early times in the formation of the galaxy, during a period of time known as "merger epoch", followed by less frequent and less massive mergers at later times. Its most prominent merger event can be associated to the Gaia-Enceladus merger. This is the last major merger of the MW, first identified by Chiba and Beers, 2000 (see also Brook et al., 2003), and popular for the large amount of debris found in the stellar halo within the solar neighbourhood, its slight retrograde motion tendency, and the significant impact on the early galactic disk, among others. A late merger of this simulation can also be identified as an analogue for the Sagittarius dwarf galaxy, that constitutes and ongoing merger event. As a third example, the simulation also shows an ongoing merger event at z = 0.02, which could be related to the interaction between the Milky Way and its closest and more massive satellite, the Large Magellanic Cloud. The first two examples are covered in further detail in the next section, where we present the sample of mergers that have been selected for the analysis. It is important to consider that these analogues hold a degree of uncertainty with observations, having slightly different properties, such as their masses, accretion redshifts, or composition (Brook et al., 2020). Additionally, this analysis is not meant to exactly reproduce the observations, but rather to study the phenomenology associated to these similar merger events.

Chapter 4

Methodology

In this chapter, we explain the procedure followed to fulfil the goals stated in section 2. First, it is described the sample of mergers used for the study, going through an overview of their main properties. Next, we give a brief explanation of the methodology used in a previous work to identify and trace the different mergers and accreted stars through the simulation, that has been applied here to build up our list of mergers. Thirdly, we describe the bases of the kinematical analysis in terms of velocity and Integrals of Motion.

4.1 Sample of mergers

The analysis has been done using a sample of 8 mergers with 7 different accretion times, out of a list of ∼20 mergers that have been analysed in less detail. The stellar masses of the selection range from 9.9×10^6 $M_\odot$ to 3.6×10^8 $M_\odot$. The main features of these satellite galaxies are shown in table 4.1, where the first column indicates the number of the row, the second column contains the label that identifies each merger, the third column presents the number of stars that they have, the fourth column exposes their stellar mass right before their accretion, and the last column presents the redshift interval in which the satellites are accreted into the main galaxy. The labels or tags that have been given to the mergers refer to the snapshot and halo identifier in the moment before the accretion takes place. For example, tag "80-2" defines a merger whose halo number is 2 in the snapshot 0080 of the simulation, that corresponds to a redshift of 5.53. In the contiguous snapshot, at redshift 4.79, this merger is recorded as part of the central galaxy.

The mergers are classified in two categories with respect to their time of accretion: early and late mergers. The former are listed in the first four rows of table 4.1, while the latter are listed in the second part of the table. This division is established according to the last major merger of the simulated MW, i.e. the Gaia-Enceladus analogue, in the way that the groups of stars accreted before this event are designated as "early mergers". Likewise, those satellites with posterior accretion times are assigned as "late mergers". As we can see, this large merger, presented in the 3rd row of the table and labelled as "176-2", is the most massive body of the sample and corresponds to the previously mentioned Gaia-Enceladus analogue of the real MW, that is referred to as GEa hereafter. Several studies agree that this object was accreted around 10-11 Gyrs ago (Helmi et al., 2018; Gallart et al., 2019; Chaplin et al., 2020), with an initial mass of $5 \times 10^8 - 5 \times 10^9$ $M_\odot$ (Helmi et al., 2018; Belokurov et al., 2018; Mackereth et al., 2019; Vincenzo et al., 2019), and dominates the inner regions of the galactic halo, in the solar

neighbourhood. These parameters differ slightly from the ones in our simulation, where the analogue merged about 11 Grys ago, with an initial mass of 3.6×10^8 $M_\odot$. Here, the debris left by its progenitor resides in a spheroidal-like structure at redshift zero, with its maximum stellar density around 10 kpc, and extends up to ~ 80 kpc from the centre.

Most of the mergers in the sample (and traced through the simulation) belong to the so-called "merger epoch" of the mock galaxy, that ended roughly 9 Gyr ago ($z \sim 1.50$), characterised by a large and violent accretion activity at high redshift. On the other hand, the mergers in the 6th and 7th rows of the table are two of the most massive found at the latest times. These are part of a more quiescent accretion period, as expected at lower redshift (e.g. Blumenthal et al., 1984; Conselice, 2014; Grand, Gómez, et al., 2017). Specifically, the merger labelled as "496-92" is the late satellite similar to the Sgr dwarf galaxy, that had its first passage into the Milky Way around 5.7 Gyrs ago (Ruiz-Lara et al., 2020) (6.85 Gyrs ago in our simulation). As expected, its morphology in the simulation at the current time shows a quite disrupted structure formed by filaments that surrounds the galactic disc in orbits of large eccentricity.

	Merger label	**nº of stars**	**$M_\star$ ($\times 10^6$ $M_\odot$)**	z_{acc}
1	80-2	513	25.74	5.53 - 4.79
2	128-11	1194	54.42	3.79 - 3.42
3	176-2	7781	355.12	2.87 - 2.65
4	176-20	1179	56.41	2.87 - 2.65
5	256-46	600	25.54	2.00 - 1.88
6	496-92	414	15.82	0.87 - 0.82
7	608-21	323	12.40	0.59 - 0.56
8	976-62	267	9.90	0.05 - 0.03

Table 4.1: Selection of early and late mergers, accreted before and after the Gaia-Enceladus analogue. The columns represent: the row number, the labels of the mergers, number of stars, stellar mass prior to their accretion, and redshift interval of infall, respectively.

According to the results from the previous project (García Bethencourt, 2020), the early mergers are found within the inner parts of the galaxy in spheroidal-like structures at the current age of the Universe. More massive early mergers dominate these inner regions in similar structures and appear rather dispersed within the main system. On the contrary, satellites that are accreted at later times tend to be more scattered towards the outer regions of the galaxy and present structures with less spherical symmetry (formed by streams in some cases). However, it is important to consider that all these final distributions are strongly dependent, not only on the times of infall and their masses, but also on the angle of accretion and initial velocities.

4.2 Mergers and stars throughout the simulation

In the sections below, we describe the methodology followed to identify and characterise mergers and accreted stars in the snapshots of our simulation. Some examples of stellar distributions in coordinate space are also given for different moments of time.

4.2.1 Identification of satellite galaxies and definition of accretion time ("Old-Star method")

The sample of mergers exposed in the previous section is a result of the study done in García Bethencourt, 2020. In this work, we took an initial configuration of the simulated galaxy at different redshifts, starting from z = 5.53 (time of 1.09 Gyrs), to identify and trace its satellite galaxies in coordinate space throughout the different snapshots, all the way to their time of accretion into the central galaxy.

The process to characterise the mergers at the time right before they are accreted starts with the identification of all satellites (or halos) in the different snapshots. This is done by determining their halo number in each timestep, which is an identifier of individual high density regions within the simulation, based on the `AMIGA Halo Finder` (or `AHF`) code (Gill et al., 2004; Knollmann and Knebe, 2009). We only identify halos with more than 20 stellar particles, more than 50 dark matter particles, and located within a radius of ∼326 kpc. This value is computed as the maximum radial distance of all dark matter particles in the main halo, also named as halo 1.

Halo numbers change from one snapshot to the next, since they are defined according to the number of particles of each halo and they might gain particles when they merge together with other satellites, or lose them due phenomena such as tidal stripping. Hence, the following step consists in recording the identification or "iord" number of the oldest star placed at the centre of each satellite galaxy. These stars represent fixed points of reference to our halos, because they are expected to be part of them for long periods of time. Thus, it is possible to search for these stars in every halo of the simulation at any time, and determine the number of their host satellites. In this way, the trajectories of the orbiting galaxies can be tracked around the central system while they merge other minor halos and become larger systems with several tracer stars residing within them. They are followed up to the time they start becoming part of the halo 1, i.e. their accretion time. In this way, mergers are defined as the group of stars that belong to each satellite in the moment right before their tracer stars are accreted. The halo number of each satellite, stellar mass, and "iord" number of all its constituent stars are recorded in this moment.

This method bears particular uncertainties in the characterisation of the mergers because of the disruption of their progenitors before the accretion. Hence, the stars closer to the main galaxy could be accreted before those located on the other side of the object at issue. Consequently, the tracer stars might infall into the central system, while other stars belonging to the same satellite remain in the outskirts, but still the satellite is recorded as merged. This issue is more flagrant for late mergers as they have a more distorted morphology. An approximation to detect and confirm that satellites are actually accreted is to search for another old star in its centre before the accretion and trace it to the next timestep. In this way, we can ensure that at least half of the satellite if fully merged, since the new star is not likely to have moved much with respect to its companions between one snapshot and the following.

4.2.2 Finding mergers within the simulation in any timestep

Mergers can be traced to different snapshots by using only the identification numbers of their stellar particles, i.e. their "iord" numbers. This can be readily done by saving those values, which are then used to construct a logical mask inside each snapshot and create "sub-halos"

associated to each merger. This is a flexible object to work with, because it is directly connected to the simulation and its properties. Therefore, it is possible to extract the value of any desired magnitude or feature of our mergers at different times to analyse their evolution, such as their spatial or velocity distributions.

It is important to have in mind that, when tracing stars belonging to mergers back in time, it is likely that most of their stars cannot be found in previous snapshots to the one that defines the merger itself (the timestep right before accretion). This is probably due to the star formation process of the simulation, meaning that those missing stars have not been born yet at those early times. Also, the majority of mergers are made of groups of other minor earlier mergers. Accordingly, they can appear as spatially separated individual satellites long before they form a single correlated structure.

Distribution of mergers before and after accretion

Applying the method and tools presented in 4.2.1 and 4.2.2, we are able to characterise any merger or group of stars at any time. To offer an example, we present the spatial distribution of two mergers at different redshifts in panels of 100x100 kpc in figures 4.1 and 4.2. Particularly, we show the stars of merger "80-2" covered in purple dots in the first figure, and the stars of merger "176-2" (GEa) coloured in gold yellow in the second figure. There are three different steps displayed in the figures, namely, the snapshot before their accretion in the first column, the snapshot right after their accretion in the middle column, and the snapshot corresponding to the present-day, i.e. at z = 0.02, in the last column. The first row of each figure represents the galaxy in a face-on view, while the second row represents the system viewed edge-on.

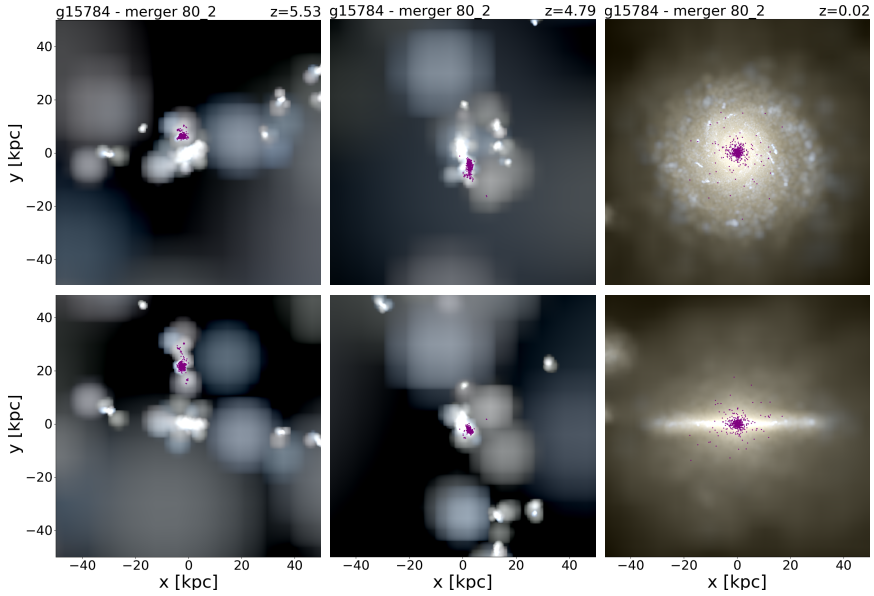

Figure 4.1: Spatial distribution of merger "80-2" in three different snapshots: before its accretion (z = 5.53), after its accretion (z = 4.79), and at the present-day (z = 0.02). The first row shows the system in face-on orientation, while the second row represents the side-on orientation.

It can be seen that both mergers have a distorted morphology during their infall, which seems a to be a more violent process for "176-2", due to its larger mass. In this case, the distribution

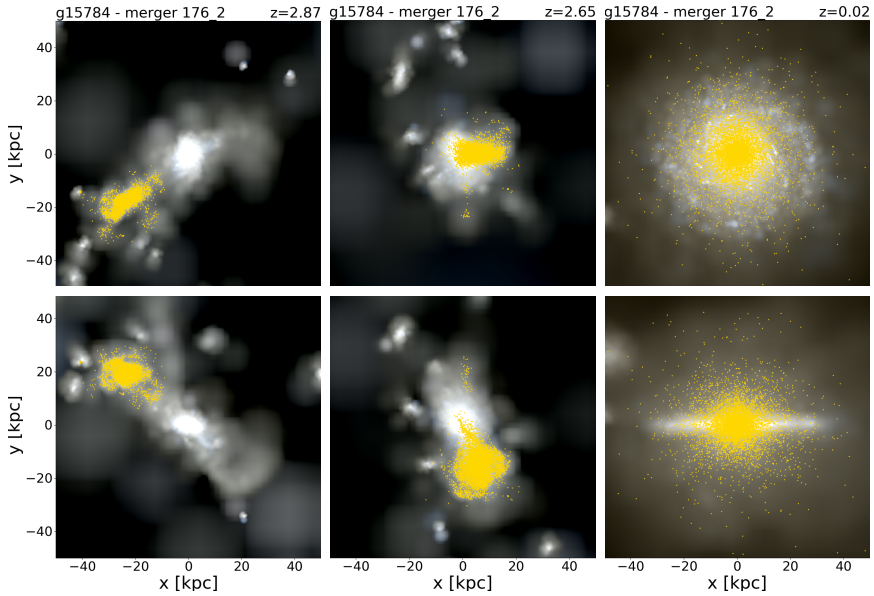

Figure 4.2: Spatial distribution of merger "176-2" (GEa) in three different snapshots: before its accretion (z = 2.87), after its accretion (z = 2.65), and at the present-day (z = 0.02). The first row shows the system in face-on orientation, while the second row represents the side-on orientation.

of stars is greatly scattered across stellar halo and its disruption is ongoing after its accretion to the central galaxy, with the accretion/disruption process lasting several timesteps. At redshift zero both mergers finally reach a stable situation and their morphology approaches spheroids that dominate the inner regions of the spiral galaxy.

4.2.3 Characterisation of total distribution of accreted stars

Generally, all groups of ex-situ stars form a distinct distribution from that of in-situ stars inside the galaxy. Not only they are found in different regions, but also they tend to have different kinematics and energies than their in-situ partners. The distribution of accreted stars is defined here as the union of all mergers that have been accreted into the galaxy from a redshift of z = 5.53 to the present day, at z = 0.02. Given that different satellite galaxies merge at different times, it is needed to identify the distribution of accreted stars at each snapshot. This distribution represents the overall population of accreted stars into the galaxy, growing in number of particles and size, and varying its properties over time as more mergers gather together.

4.3 Kinematical analysis

Kinematics and energy states are commonly used to search for correlations in stellar groups and to describe them at a certain time, as well as for giving an estimate of which galactic component they belong to. Here, we focus on velocity space and the Integrals of Motion.

4.3.1 Velocity space

Velocity space refers to the relation between the different velocity components in the 3-dimensional space, namely: the cylindrical radial velocity in the x-y plane v_{Rxy}; the cylindrical

tangential velocity in the x-y plane, v_{Cxy} (or azimuthal velocity, v_ϕ); the vertical velocity to the x-y plane v_z; and the spherical radial velocity v_{rad}. All of them are given in units of kilometers per second.

The components defined in cylindrical coordinates are easily computed from the positions and velocities in cartesian coordinates. These calculations are presented below, for v_{Rxy} and v_{Cxy}, respectively:

$$v_{Rxy} = \frac{dr_{xy}}{dt} = \frac{2x\dot{x} + 2y\dot{y}}{2\sqrt{x^2+y^2}} = \frac{x\dot{x} + y\dot{y}}{r_{xy}} = \frac{xv_x + yv_y}{r_{xy}} \tag{4.3.1}$$

where $r_{xy} = \sqrt{x^2+y^2}$ is the radial distance to the centre of the system in the x-y plane (i.e. face-on view of the galaxy), and $\dot{x} = \frac{dx}{dt} = v_x$, $\dot{y} = \frac{dy}{dt} = v_y$ are the corresponding velocity components in cartesian coordinates. On the other hand, given that the total velocity in the x-y plane is $v_{xy} = \sqrt{v_{Cxy}^2 + v_{Rxy}^2} = \sqrt{v_x^2 + v_y^2}$, then:

$$\begin{aligned} v_{Cxy}^2 &= v_{xy}^2 - v_{Rxy}^2 = (v_x^2 + v_y^2) - v_{Rxy}^2 = (v_x^2 + v_y^2) - \left(\frac{xv_x + yv_y}{r_{xy}}\right)^2 = \\ &= \frac{(v_x^2 + v_y^2)r_{xy}^2 - (x^2v_x^2 + y^2v_y^2 + 2xv_xyv_y)}{r_{xy}^2} = \\ &= \frac{x^2v_y^2 + y^2v_x^2 - 2xv_xyv_y}{r_{xy}^2} = \frac{(xv_y - yv_x)^2}{r_{xy}^2} \end{aligned} \tag{4.3.2}$$

Therefore, the circular velocity is given as:

$$v_{Cxy} = \frac{xv_y - yv_x}{r_{xy}} \tag{4.3.3}$$

Finally, the spherical radial velocity is simply defined as $v_{rad} = \sqrt{v_{Rxy}^2 + v_z^2}$. Thus, it can be directly computed from the result in 4.3.1 and the vertical velocity component. The total radial velocity is specially used to obtain the so-called Toomre diagram, that relates v_{rad} to the azimuthal velocity, v_ϕ. The Toomre diagram is an useful tool to determine whether the movement of stars follow the galactic rotation or have a higher amount of random motion, i.e. to know to which galactic component stars are more likely to belong to (bulge, stellar halo, thin disk, thick disk).

In this project, we have obtained and analysed the following velocity space diagrams for each one of the mergers presented in table 4.1: v_{Cxy} with respect v_{Rxy}, v_{Cxy} with respect v_z, v_{Rxy} with respect v_z, and v_{rad} with respect v_ϕ.

4.3.2 Integrals of Motion

The IoM is another popular parametric space used to study stellar accretion in galaxy research. In an ideal system, the integrals of motion (energy and angular momentum) are supposedly conserved quantities. Nevertheless, in a system such as the Milky Way, whose potential energy grows over time due to the continued accretion of matter, the total energy cannot be conserved. However, it is expected that remnants of past mergers appear clustered in this space. Hence, this

useful tool also provides certain correlations for individual mergers, allowing to identify accreted structures according to the position and shape of these distributions.

The space of Integrals of Motion is mainly defined by the vertical and perpendicular components of the angular momentum, L_z and $L_\perp = \sqrt{L_x^2 + L_y^2}$, and the total energy, E. The $L_\perp$ component is sometimes convenient to select distinct stellar substructures (Helmi and White, 1999; Helmi and Tim de Zeeuw, 2000) in the space formed by L_z and $L_\perp$, or the space given by $L_\perp$ and E. In this work, we focus on the relation between the specific energy and the vertical component of the specific angular momentum, i.e. both divided by mass, and represented as E and j_z, respectively. The energy is given in units of $\mathrm{km}^2/\mathrm{s}^2$, and the z-component of the angular momentum in units of kpc km/s. The total specific energy is calculated as the sum of the kinetic energy and the potential energy of the stars, divided by the mass. This is:

$$E' = \frac{1}{2}v^2 + \Phi(r) \tag{4.3.4}$$

where the square of the total velocity is $v^2 = v_x^2 + v_y^2 + v_z^2$.

Normalisation of total energy

To obtain the diagram that relates E with j_z, the total energy is normalised to the maximum total energy of all stars in the main central galaxy. This is done by subtracting this maximum value to E' (see expression 4.3.4). Therefore:

$$E = E' - E_{max}(h[1]_{stars}) \tag{4.3.5}$$

where $h[1]_{stars}$ represents all stars contained in halo 1.

Hence, the maximum total energy of fully bound stars is zero. The more negative are the values of E, the more bound are stars to the galaxy. Analogously, positive values of the total energy correspond to stars or groups of stars that are not part of the main galaxy, and they can be considered different separate systems energetically. This normalisation is carried out thanks to an algorithm implemented in the Pynbody package, given by the `pynbody.analysis.decomp` function.

Chapter 5

Results and Discussion

This chapter is destined to the exposition and discussion of the results attained from the analysis described in previous sections. As mentioned before, we focus on the phase space plots drawn from a selection of 8 representative mergers to expose in the following pages. Besides, we discuss the contribution of mergers to the inner regions of the stellar halo and their density profile at redshift zero. Lastly, it is exposed the temporal evolution of the radial distance of mergers prior to their accretion, and its relation to their star formation history, especially for late mergers with several pericentric passages.

5.1 Evolution of mergers in phase space

We present the mergers in a range of redshifts from 4.23 to 0.02 to analyse their evolution. Their density distributions in phase space are represented as coloured contours in each panel, where the darker lines refer to lower density of data points and the lighter contours represent higher densities. As a greyscale background of contours it is shown the distribution of all accreted stars at each time in every space. In this case, the darker regions mean higher density of particles and vice versa.

Generally, the phase space distributions of the mergers are initially more compact structures and gain larger dispersion as time goes by. This is due to their phase space mixing within the galaxy during their evolution. Analogously, all accreted stars also show this behaviour, but their evolution depends on its growth via other mergers as well. This background distribution varies more slowly from z = 1.48 to z = 0.02, and shows a significant decrease in total energy as well, due to the deepening of the potential well of the system. This means that the "merger epoch" has finalised and the galaxy's dark matter halo has eventually virialised.

Merger "80-2". It is the earliest merger of the analysis, whose velocity and IoM spaces are shown in figures 5.4 and 5.5. This object is accreted at redshift 5.53 and its evolution inside of the main galaxy starts at redshift 4.23 (first panel of odd rows). Its phase space shows random distributions of velocities that remain centred around zero in the course of the evolution, i.e. velocities are small in average. Also, there seems to be a similar amount of stars with prograde (v_{Cxy}, $v_\phi > 0$) and retrograde motions (v_{Cxy}, $v_\phi < 0$), and a similar amount of stars with positive and negative radial velocities. This situation is clearly expected for early accreted stars, since they infall into a newly formed galaxy that has not entirely developed a disk to induce enough rotation in the surrounding material. Hence, these stars follow halo-like kinematics during most

of their evolution, except for a slight increase in rotation towards later times (see second-to-last and last panels of the 2nd and 4th row of figure 5.4, and of second row in figure 5.5), due to the gravitational pull of the more developed galactic disk. As for the space of Integrals of Motion, which is shown in the last two rows of figure 5.5, we can verify that the merger is already bound to the main system in the first panel, since it is found at negative energies. It can also be seen that it loses energy in time, becoming a more bound part of the galaxy. The mean value of this loss is around 2.2×10^5 km^2/s^2, but the range of energies also increases largely at late times.

Merger "128-11" is accreted between z = 3.79 and z = 3.42, and its phase space can be seen in figures 5.6 and 5.7. It has some similarities with respect to the GEa (described in the subsection below) in terms of their shape in phase space. This resemblance is mainly seen in the elongated structure in the space defined by v_{Cxy} and v_{Rxy}, and in the Toomre diagram, where the merger shows a narrow range in circular velocities and a longer range of radial velocities. In this case, the shape is due to large values of v_{Rxy} and little rotation before the accretion[1] Another feature of this body is its erratic evolution in the first three timesteps (especially in the v_{Rxy} versus v_z space, and IoM space), which could be the consequence of a highly violent accretion activity at those times added to the initially large radial velocities in the x-y plane. Despite of being an early merger, it barely loses energy over time in average compared to other mergers with similar infall times. As we can see in the last rows of figure 5.7, the energy loss is roughly 1.0×10^5 km^2/s^2, and the distribution maintains high energies at z = 0.02, meaning that this merger is currently weakly bound to the main system. Here, there are also some similarities with the GEa in terms of shape, although "128-11" is found at slightly higher energies.

Merger "176-2". The Gaia-Enceladus analogue of this simulation, accreted at z = 2.87, is shown in figure 5.8. The contours present an elongated shape along v_{Rxy} at all times, as it is expected for this object. This is the result of a polar accretion orbit, in which the merger has large velocities in the perpendicular direction to the galactic plane before the infall, so that it is barely influenced by the rotation of the disk[2]. These stars are likely to have highly eccentric orbits within the galaxy (Brook et al., 2003). As the simulation evolves, this large object maintains most of this shape and becomes more stable and mixed. From the analysis of our results, we can verify that the progenitor of this body was counter-rotating before its infall, since the distribution is found at negative values of the circular velocity component at that time. A fraction of this retrograde motion is kept until z = 0.02, where there is a certain dispersion of stars with negative v_{Cxy} and j_z. This configuration at the present day is also concurrent with the findings that suggest that there are stars with retrograde motions associated to the real Gaia-Enceladus structure in the stellar halo (Villalobos and Helmi, 2008; Villalobos and Helmi, 2009). In addition, the high binding energy of this merger during its evolution suggests that many of its stars are part of the outer halo, which is also thought to have a high proportion of retrograde orbits due to the debris from this merger and from other structures, such as Sequoia (Helmi et al., 2017; H. H. Koppelman et al., 2019). The grayscale distribution in the last step of the IoM space indicate, indeed, that the stellar halo has a higher fraction of retrograde motions for more weakly bound stars than for lower energy stars at z = 0.02 (the dispersion is larger at higher energies). As we can see in the last column of the figure, the region defined by this structure agrees with results from other studies (e.g. Massari, D. et al., 2019; H. H. Koppelman et al., 2019; Ruiz-Lara et al., 2022), despite of being limited to the solar neighbourhood in

[1]Merger "128-11" is around (v_{Cxy}, v_{Rxy}, v_z) = (14, 81, -35) km/s in the timestep before its accretion.
[2]Merger "176-2" is around (v_{Cxy}, v_{Rxy}, v_z) = (-51, -182, -92) km/s in the timestep before its accretion.

observational research.

Merger "176-20" is displayed in figure 5.9. This object infalls into the central galaxy at the same time than the GEa, but shows an entirely different structure in phase space. Its velocity space indicates a larger amount of random orbits than the previous two mergers during the evolution. We can observe that this merger starts with a mean retrograde motion and shifts to positive circular orbits as it evolves, but leaves a certain debris of retrograde stars. Regarding to its energy, it is clearly more bound than mergers "128-11" and "176-2" from the beginning to the present day, with a mean total energy around -2.0×10^5 km^2/s^2. Therefore, this stellar structure is more likely to be found in more inner regions of the halo than "128-11" and "176-2".

Merger "256-46". This is the most retrograde merger found in the sample from its accretion, at z = 2.00, to the present day. It can be seen in figure 5.10 that it presents an elongated structure along v_{Rxy} (mainly positive values at z = 1.48), while has little velocity dispersion in v_z and a narrow range of circular velocities. This rotation is small ($v_{Cxy} \sim -16$ km/s) at the beginning and seems to become more negative with time, instead of engaging with the galactic disk's motion. This could also be a consequence of the large radial velocities during the accretion, that counteract the rotational velocity induced by the disk.[3] Like for other late mergers, the space of the Integrals of Motion shows the high energies of this stellar group, located in the retrograde part of the plots. In fact, this distribution has great similarity with the Sequoia structure in this IoM space (e.g. see Figure 2 from Massari, D. et al., 2019), where it is positioned around (j_Z, E_T) = (-1×10^3 kpc km/s, -6×10^4 km^2/s^2) at z = 0.02.

Merger "496-92". As it has been previously mentioned, this is the Sgr merger analogue of this simulated Milky Way. Its evolution in velocity space and IoM space is shown in figure 5.11, where the distribution is observed to vary rapidly over time, especially in the space represented by v_{Rxy} and v_z. This abrupt development indicates the sudden changes in radial velocities due to the strong pull that this late merger suffers by the main galaxy, which is also associated to its ribbon-shaped morphology in coordinate space. On the contrary to other mergers, the velocity dispersion in the different components does not grow with time, but decreases instead, resulting in a distribution with a narrower range of velocities at the end. In this case, the rotational motion of the satellite is clearly prograde. In the last row of figure 5.11, we can see that this body is also weakly bound at the present day, and its average value of total energy is above -0.5×10^5 km^2/s^2. From what has been discussed in the previous lines, these results verify the ongoing accretion situation of "496-92", given that it is not fully mixed within the galaxy at the present time and forms a distinct group in the stellar halo according to its kinematics. On the other hand, its mean j_z (around 6000 kpc km/s) is larger than in other studies, where this value tends to be below 2000 kpc km/s (e.g. Massari, D. et al., 2019; Ruiz-Lara et al., 2022).

Merger "608-21". This late merger, presented in figure 5.12, is a highly prograde structure and also displays strong variations in phase space during the evolution. The contours show a compact distribution in the first three steps and become more extended at the end, where their shape and position point out that some stars might have similar properties than those belonging to the thick disk, e.g. clear prograde rotation (and certain amount of stars with $v_{Cxy} > 200$ km/s), and small dispersion in v_z. However, it is a weakly bound stellar structure, since it is found at very high energies, near to the maximum of energy associated to the main galaxy.

[3] Merger "256-46" is around (v_{Cxy}, v_{Rxy}, v_z) = (-12, 114, 66) km/s in the timestep before its accretion.

Merger "976-62", accreted into the simulated MW at z = 0.05, is shown in figure 5.13. As it can be seen in the figure, this merger has an overall retrograde motion, positive vertical velocities, and the variation in radial velocity is small. Therefore, despite of being the latest merger of the sample, it does not align with the rotation of the galactic disk. On the other hand, because of the late time of infall, there is no much variation of the distribution between the two timesteps displayed for all the spaces. As for the panels representing the IoM, these show the stellar distribution at high energies, and a large range of j_z, distinctive for late mergers.

5.1.1 Comparison between early and late mergers in phase space

These results, along with the characterisation of some additional satellites, show that early mergers generally have a more random motion and no predominant rotation during their evolution (especially at z = 0.02), whilst late mergers tend to be aligned with the disk and have narrow ranges of circular velocities. However, it is essential to take into account for these final distributions the direction in which they are accreted, since they could maintain a retrograde behaviour (e.g. merger "256-46") or be barely induced by the disk's rotation (e.g. merger "176-2"). Moreover, the rotation seen in late mergers could be caused by other phenomena apart from the dynamical friction of the disk, such as a bias in the large scale structure or the torque of the galactic disk. On the other hand, early mergers are expected to be strongly bound inside of the main galaxy at the present day (average total energy generally below -2.0×10^5 km^2/s^2, since they are closer to the bottom of the gravitational well of the central halo when they are accreted. Nevertheless, there are some exceptions such as mergers "128-11" and "176-2", that are found in $-2.0 \times 10^5 < E_T < -1.0 \times 10^5$ km^2/s^2. In contrast, late mergers are found at high energies (mean total energy above -1.0×10^5 km^2/s^2), being close to the bound limit of the system as they fall from larger distances into the MW-like galaxy. These outcomes agree with the fact that those mergers with early times of infall are part of/tend to be concentrated in the inner regions of the stellar galactic halo (although these might have a variety of energies, but generally lower than -1.0×10^5 km^2/s^2), while mergers with posterior times of accretion are part of the outer part of the stellar halo. Additionally, early mergers are more stable structures, due to their longer evolution inside of the galaxy, being able to get mixed up with the main system and adopting a variety of velocities. On the contrary, late mergers have a shorter evolution in the galaxy and conserve a great amount of their original motion. This is seen in velocity space, where later mergers form more distinct structures, whilst early mergers show larger scattering.

5.1.2 Influence of Gaia-Enceladus on early mergers

The redshift interval of accretion of the GE-analogue is z = 2.87 - 2.65. The total mass ratio between this massive object and the main galaxy at redshift 2.87 is 0.15, and it is likely to have had some impact on the orbits of previously accreted stars in the same way than for in-situ stars from the primordial thick disk. Indeed, a noticeable variation can be seen in the vertical velocity component in the figures during this time interval. For instance, in figure 5.4 the velocity dispersion of v_z increases for both, the distribution associated to the merger and the one associated to all accreted stars. In the case of merger "80-2", the variation of the standard deviation of v_z between these two timesteps is 33 km/s. This phenomenon is also seen in other early mergers of the analysis and is analogous to the thick disk heating for in-situ stars, since they seem to adopt more halo-like kinematics.

5.2 Contribution of accreted stars to the galactic bulge

To study the contribution of ex-situ stars to the bulge at the present day, we define two spherical regions within the simulated Milky Way. First, it is defined a sphere of 2 kpc of radius from the centre of the galaxy. Second, it is defined a concentric spherical layer for the area between 2 and 3 kpc from the centre. The 3rd and 4th columns of table 5.1 display the fraction of stars from each merger and the fraction of these compared to the total number of stars within the two regions, respectively. In addition, the last row shows the results for all accreted stars.

	Merger label	**Contribution to 0-2 kpc**	**Contribution to 2-3 kpc**
1	80-2	53.61% / 0.02%	14.43% / 0.05%
2	128-11	4.86% / 0.01%	4.44% / 0.04%
3	176-2	7.21% / 0.05%	7.45% / 0.40%
4	176-20	24.85% / 0.02%	19.34% / 0.16%
5	256-46	-	0.17% / -
6	496-92	-	-
7	608-21	-	-
8	976-62	-	-
9	Accreted stars	16.06% / 0.36%	8.79% / 1.64%

Table 5.1: Contribution of accreted stars to the galactic bulge. The first column indicates the number of each row, the second column presents the labels of the mergers, the third and fourth columns present the fraction of stars from each merger and the fraction of accreted stars within the total stellar bulge in 0-2 kpc and in 2-3 kpc, respectively.

As it can be seen in the table, around half of the stars from merger "80-2" are found in the inner spheroid, whilst $\sim 14\%$ of its stars are found in the outer part of the bulge. On the contrary, the rest of bodies in this sample account for smaller fractions of their stars to the more inner region.[4] The Gaia-Enceladus analogue appears to be the structure that contributes the most to both regions with respect to the total bulge compared with other mergers, although only $\sim$14% of its debris is found there. On the other hand, by comparing between mergers "128-11" and "176-20", that have similar stellar masses (see table 4.1), we notice that the former contributes much less to both parts of the bulge despite of having a higher accretion redshift. Nonetheless, this result agrees with the IoM space of both structures at $z = 0.02$, that show "128-11" at higher energies, characteristic of outer parts of the galaxy. As observed in the last column, the contribution to the total bulge is higher in its outer part for all mergers, i.e. there are more ex-situ stars in the outer bulge, rather than the inner bulge. For late mergers, the contribution is null for the innermost region, and only 0.17% of the stars from merger "256-46" can be found in 2-3 kpc. This is expected since later mergers settle in outer parts, as already discussed.

In the case of all accreted stars, 24.85% of this group is found in the bulge. However, these only constitute the 2% of the total number of bulge stars. These results imply that: 1) above 70% of accreted stars are located in more external parts of the galaxy and; 2) the vast majority of stars in the galactic bulge are formed in-situ.

[4] Other analysed early mergers contribute with $71 - 73\%$ and $\sim 14\%$ of their stars to the inner and outer bulge, respectively.

5.3 Density profile of mergers

The density profile of stars is another useful tool to analyse the distribution of mergers within the main galaxy and their contribution to the each region. In figure 5.1, we show the density profiles of all mergers in the sample as a surface density (given in $M_\odot/kpc^2$) with respect to the distance from the centre of the galaxy (in kpc) at z = 0.02. These profiles are made with 8 bins.

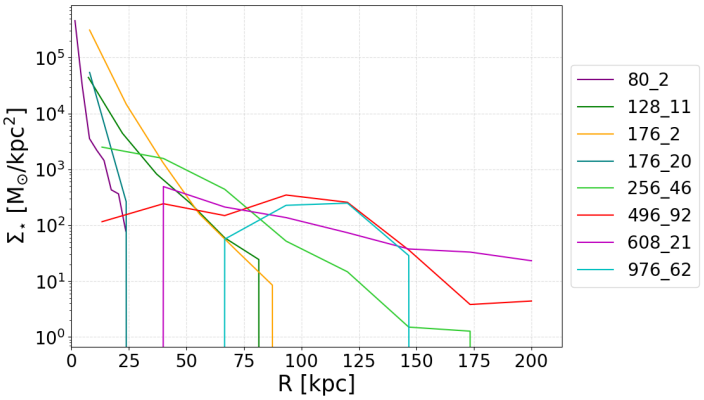

Figure 5.1: Density profiles of mergers at z = 0.02, i.e. surface density of mergers (in units of $M_\odot/kpc^2$) with respect to the distance from the centre of the galaxy (in kpc).

It can be observed in the figure that early mergers are densest near the centre, all with surface densities above 10^4 $M_\odot/kpc^2$ between 0 and 25 kpc. These densities decrease rapidly towards the outer parts of the galaxy, becoming negligible around 80 kpc. As in phase space, in this case there is another similarity between mergers "128-11" and "176-2", where their density profiles follow nearly parallel trends, having the latter merger higher density, as expected for its larger mass. On the other hand, late mergers are generally less dense in average and show flatter profiles that vary more slowly with the increase of distance, i.e. they are more scattered throughout the galaxy. Their stellar density is below 10^4 $M_\odot/kpc^2$ or negligible in the region between 0 and 25 kpc, increasing towards the outskirts for some mergers. In the cases of "496-92" and "976-62", instead having higher density near the centre, their profiles display peaks around 90 kpc and 120 kpc, respectively. This is probably due to a ring-shaped morphology caused by their late infall.

5.4 Distance of mergers before accretion and SFH

We have also explored the spatial evolution of mergers prior to their accretion in terms of their average radial distance, that varies with time as they approach to the centre of the galaxy. The results can be seen in figure 5.2, where early mergers are shown in the panel on the left, and late mergers are shown in the panel on the right. There are important differences between early and late mergers in this case as well. In the first panel of the figure it can be seen that early mergers fall directly into the galaxy, i.e. they only have one pericentric passage in which they are accreted into the simulated MW. In the second panel of the figure, the radial distance of late mergers is shown by damped oscillations, characteristic of these objects falling and circling around the galaxy. Since they are accreted at later times, they have several pericentric and apocentric passages before their infall. As we can see in the plots, the progenitor satellites of

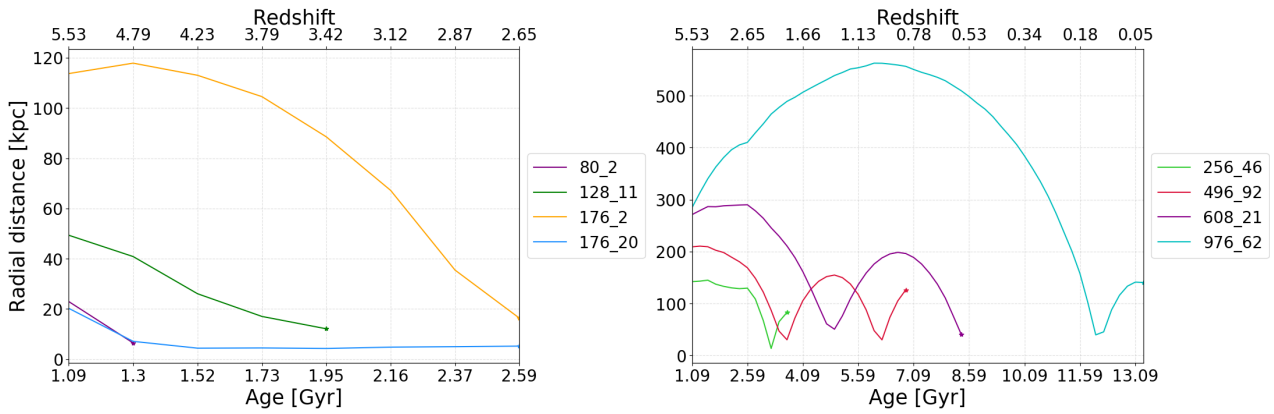

Figure 5.2: Mean radial distance (kpc) of mergers to the centre of the galaxy with respect time (Gyrs) for early mergers (left) and late mergers (right).

later mergers generally fall from larger distances than earlier mergers, which is consistent to previously discussed results.

The star formation histories (SFH) of each one of the mergers in the sample are presented in figure 5.3. The star formation rate (SFR) is given in units of solar masses per year, while time is given in Gyrs. These histograms are made with a number of 100 bins. We can see, that the star formation of early mergers shuts down soon in the evolution of the galaxy (before 3 Gyrs of evolution), due to their rapid disruption and accretion. Hence, their stellar populations are old, $\gtrsim$ 11 Gyr. Also, these early mergers show several peaks of high SFR just before their accretion. Mergers "80-2" and "128-11" seem to have their star formation is enhanced at 0.95 Gyrs and 1.05 Gyrs for the first one, and at 1.50 Gyrs for the second one, approximately. These two objects infall into the main galaxy at 1.09 Gyrs and 1.73 Grys, respectively. Therefore their gas has not been entirely stripped away during the accretion and it might suffer some compression in this process to be able to create denser regions for star formation to increase (e.g. Di Cintio et al., 2021). The same situation is found for mergers "176-2" and "176-20", where there is also an increase in the SFR from 1.75 Grys until 2.50 Gyrs, being their accretion time at 2.37 Grys. The SFR is one order of magnitude higher for the GEa, as we can see in the yellow coloured histogram, as expected due to its larger total and stellar mass.

For late mergers, their SFR is clearly lower at all times compared to previously accreted objects, denoting that they have less gas content due to the strong tidal stripping at late times. The SFR of the retrograde merger labelled as "256-46" is shown in the central panel of figure 5.3, coloured in light green. There are two narrow peaks of high star formation rate around 1.90 Grys and 3.10 Grys, which are close in time with the apocentric and pericentric passages of this object (see second panels of figure 5.2), being these ∼1.50 Gyrs and ∼3.20 Gyrs, respectively. In this case, star formation is also quenched early, leaving an old population of stars as the debris of this satellite. The rest of late mergers, have more extended SFH in time, until ∼8 Gyrs for the last two. Thus, these maintain a younger population of stars in average. For the Sgr analogue (coloured in red), the SFR is enhanced mainly around 2 Gyrs, when the satellite has already passed its first apocentric passage. Then, the star formation decays until the accretion, meaning that the object has completely lost its gas reservoir by tidal stripping (or its density has become low enough to stop forming stars). The two latest mergers, have a low and more continuous

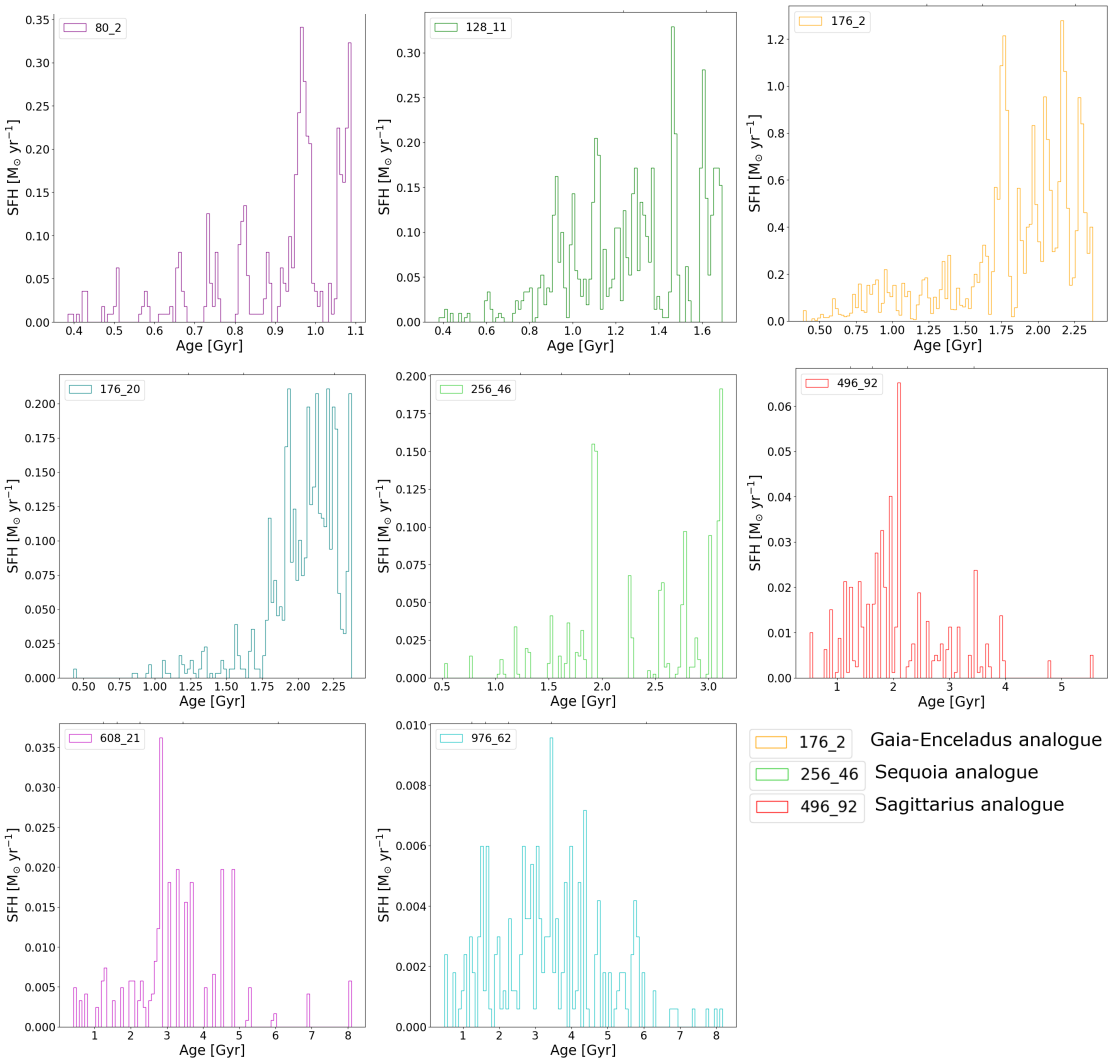

Figure 5.3: Star formation histories of mergers, given in $M_{\odot}$/yr. From left to right, and from top to bottom, each panel correspond to the following mergers, respectively: "80-2", "128-11", "176-2" (*Gaia-Enceladus analogue*), "176-20", "256-46" (*Sequoia analogue*), "496-92" (*Sagittarius analogue*), "608-21", and "976-62".

SFR with time, with peaks around 3 Gyrs, but it progressively decays before their infall into the central galaxy (several Gyrs before for the last merger displayed).

Therefore, the population of stars from early mergers is clearly older in average than the population of stars from satellites with later times of accretion. Since early mergers are mostly found in the inner regions of the galaxy, these results indicate that the ex-situ inner stellar halo is generally older than the outer one. This situation is similar to the case of in-situ stars, where the oldest ones were formed in the bulge (Tumlinson, 2009; Starkenburg et al., 2017; El-Badry et al., 2018) and younger stars were born in outer regions.

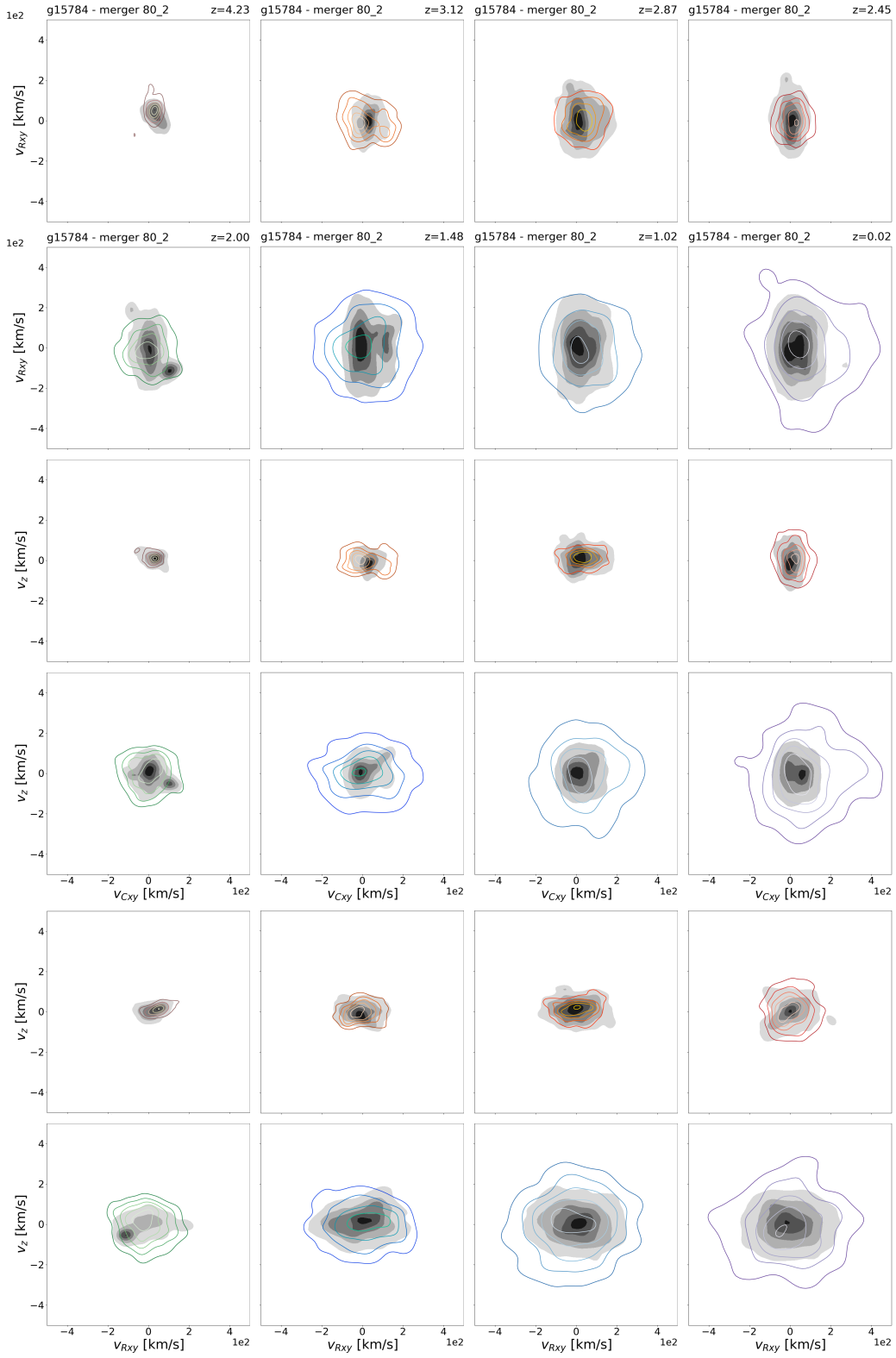

Figure 5.4: Temporal evolution of merger "80-2" in velocity spaces (v_{Cxy} vs. v_{Rxy}, v_{Cxy} vs. v_z, and v_{Rxy} vs. v_z). Each panel represent a different redshift, namely: 4.23, 3.12, 2.87, 2.45, in odd rows; and 2.00, 1.48, 1.02, 0.02, in even rows.

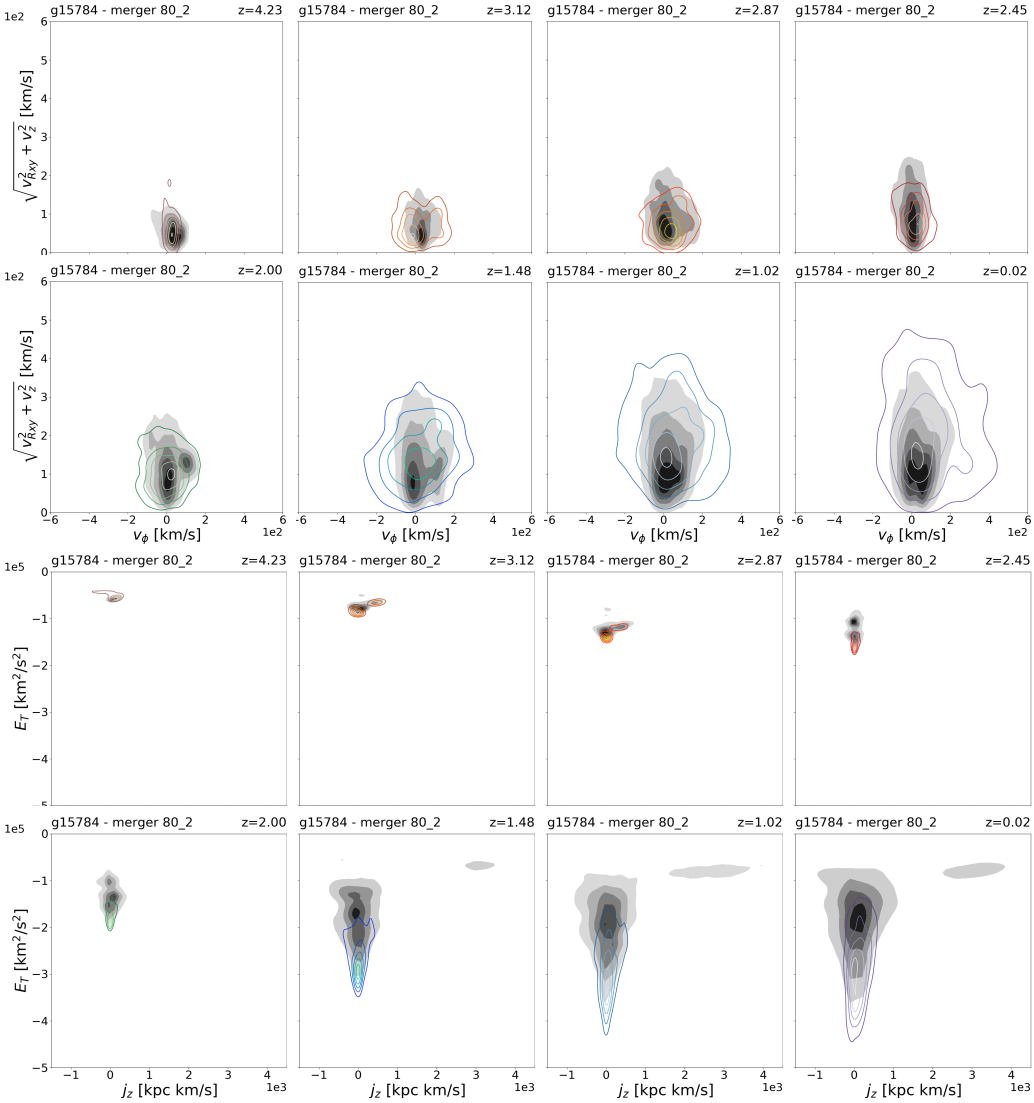

Figure 5.5: Temporal evolution of merger "80-2" in Toomre diagram and IoM space (v_ϕ vs. $\sqrt{v_{Rxy}^2 + v_z^2}$, and j_z vs. E_T). Each panel represent a different redshift, namely: 4.23, 3.12, 2.87, 2.45, in odd rows; and 2.00, 1.48, 1.02, 0.02, in even rows.

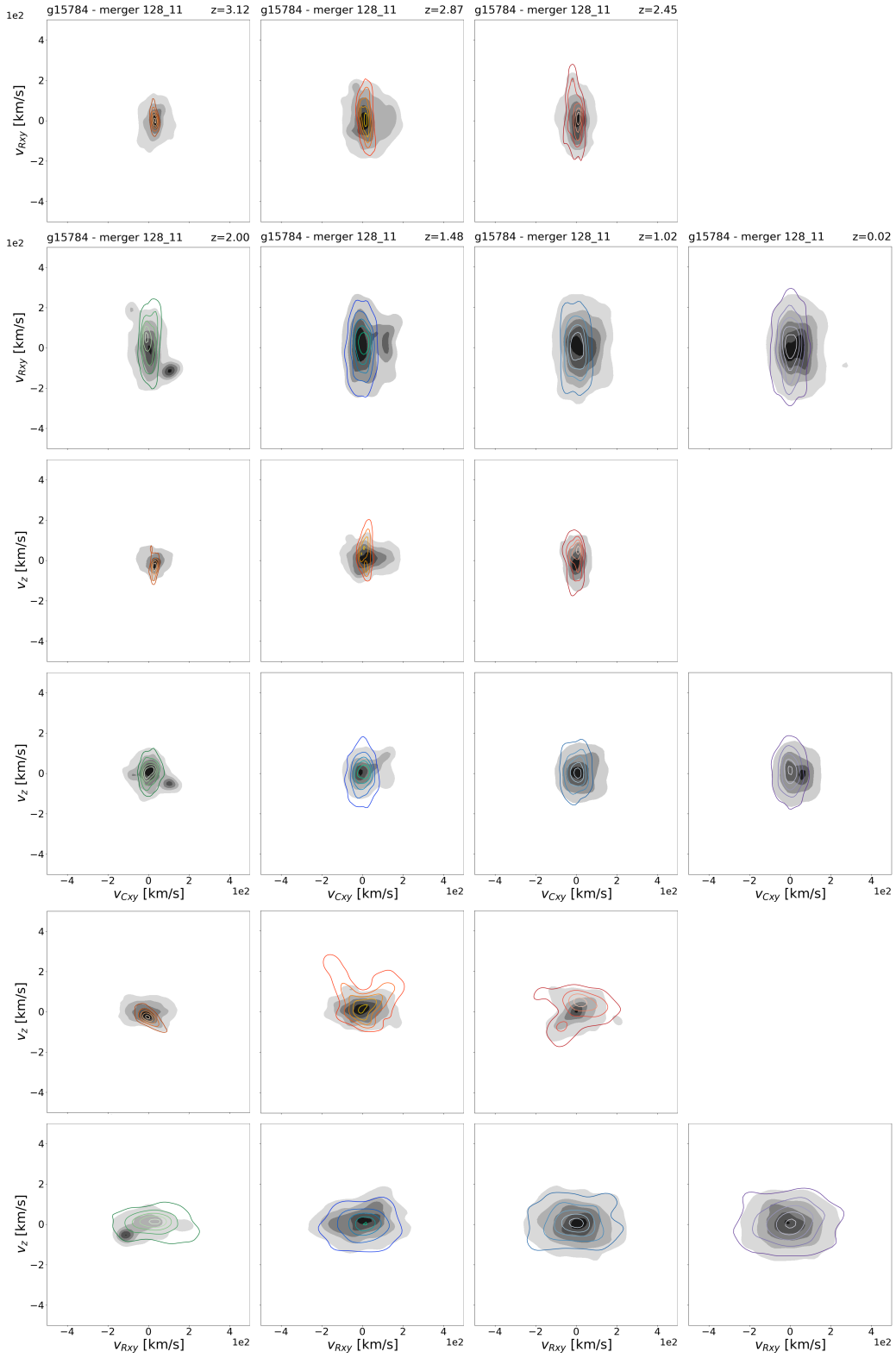

Figure 5.6: Temporal evolution of merger "128-11" in velocity spaces (v_{Cxy} vs. v_{Rxy}, v_{Cxy} vs. v_z, and v_{Rxy} vs. v_z). Each panel represent a different redshift, namely: 3.12, 2.87, 2.45 in odd rows; and 2.00, 1.48, 1.02, 0.02 in even rows.

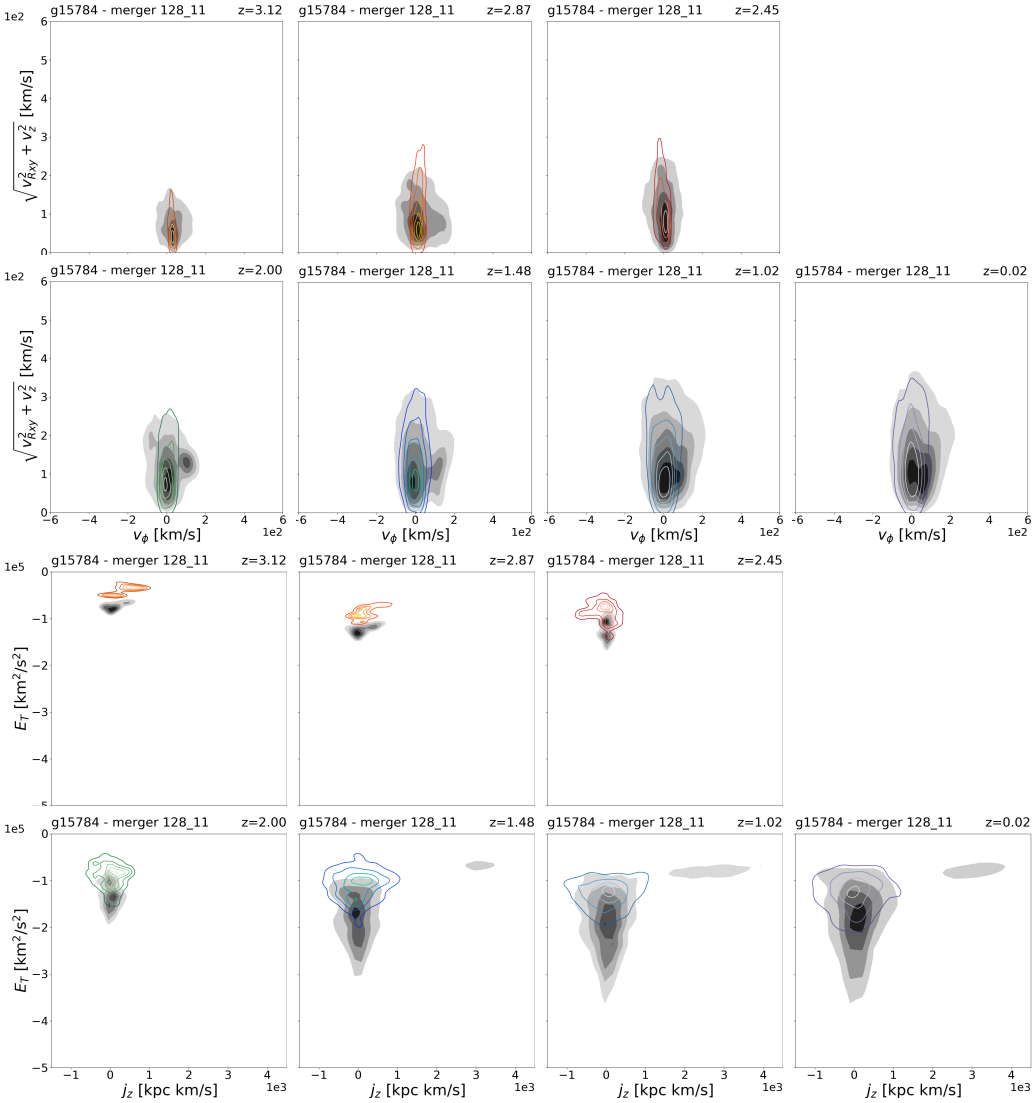

Figure 5.7: Temporal evolution of merger "128-11" in Toomre diagram and IoM space (v_ϕ vs. $\sqrt{v_{Rxy}^2 + v_z^2}$, and j_z vs. E). Each panel represent a different redshift, namely: 3.12, 2.87, 2.45, in odd rows; and 2.00, 1.48, 1.02, 0.02, in even rows.

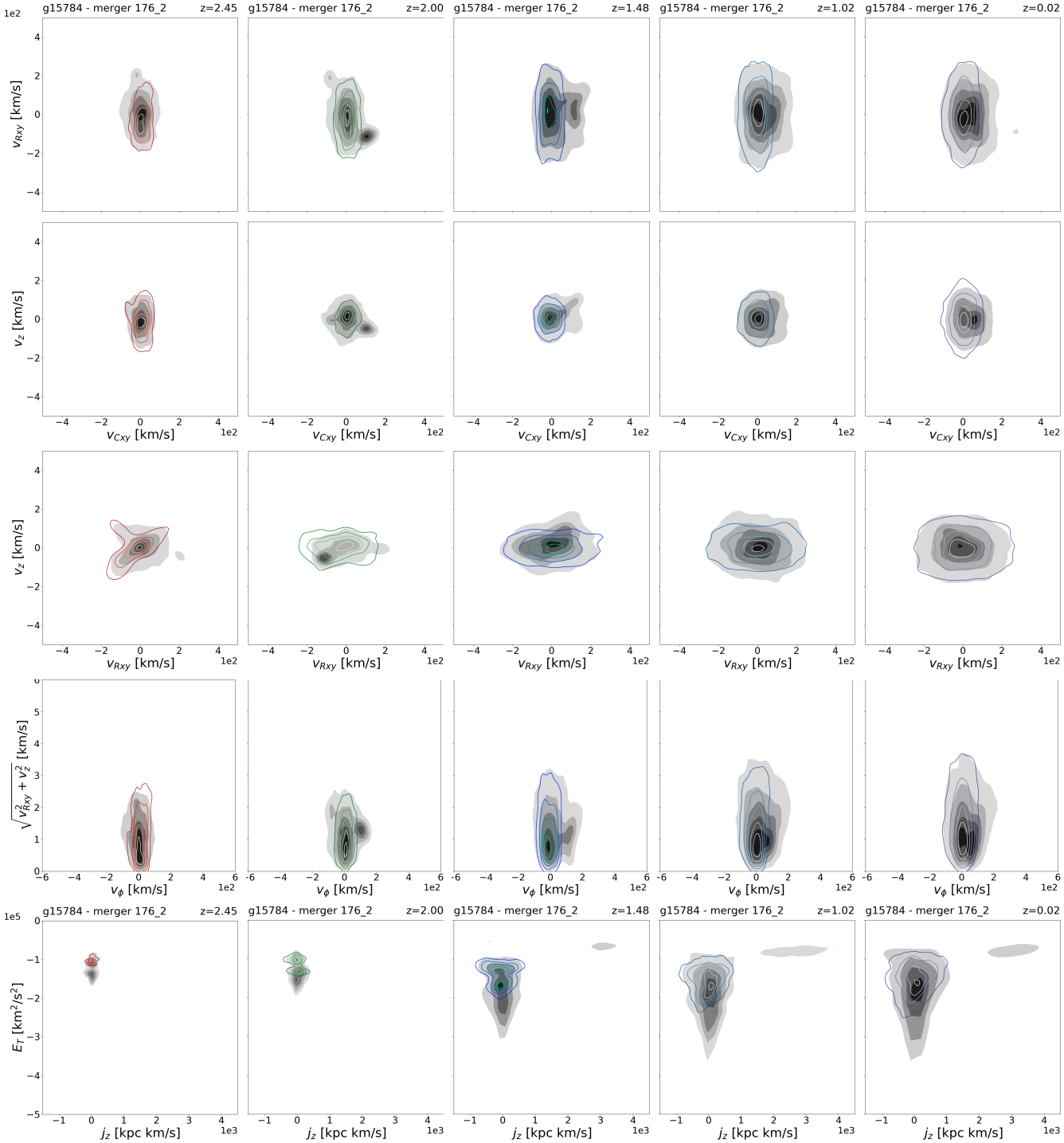

Figure 5.8: Temporal evolution of merger "176-2" (*Gaia-Enceladus analogue*) in velocity and IoM spaces. Each panel represent a different redshift, namely: 2.45, 2.00, 1.48, 1.02, and 0.02.

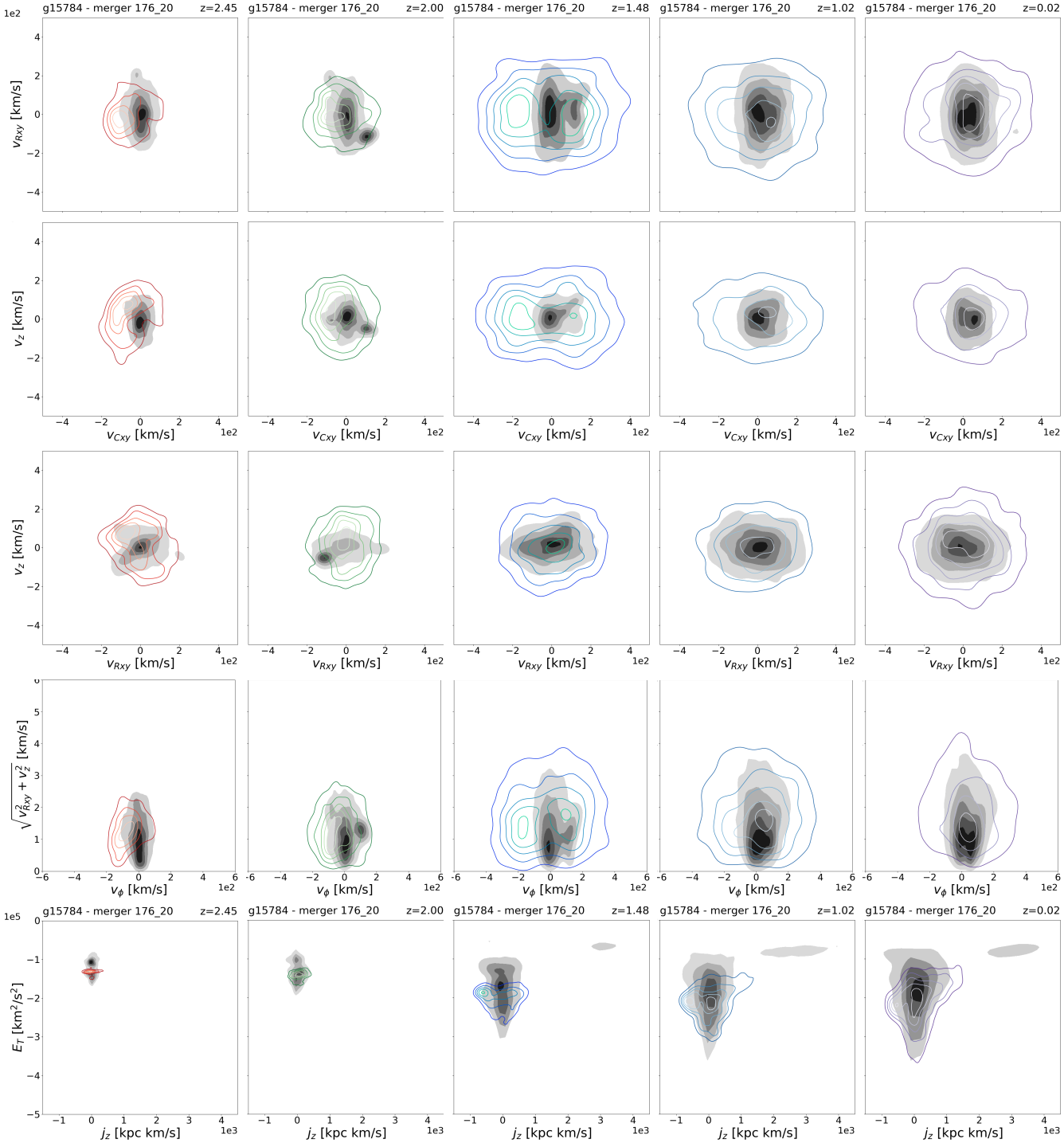

Figure 5.9: Temporal evolution of merger "176-20" in velocity and IoM spaces. Each panel represent a different redshift, namely: 2.45, 2.00, 1.48, 1.02, and 0.02.

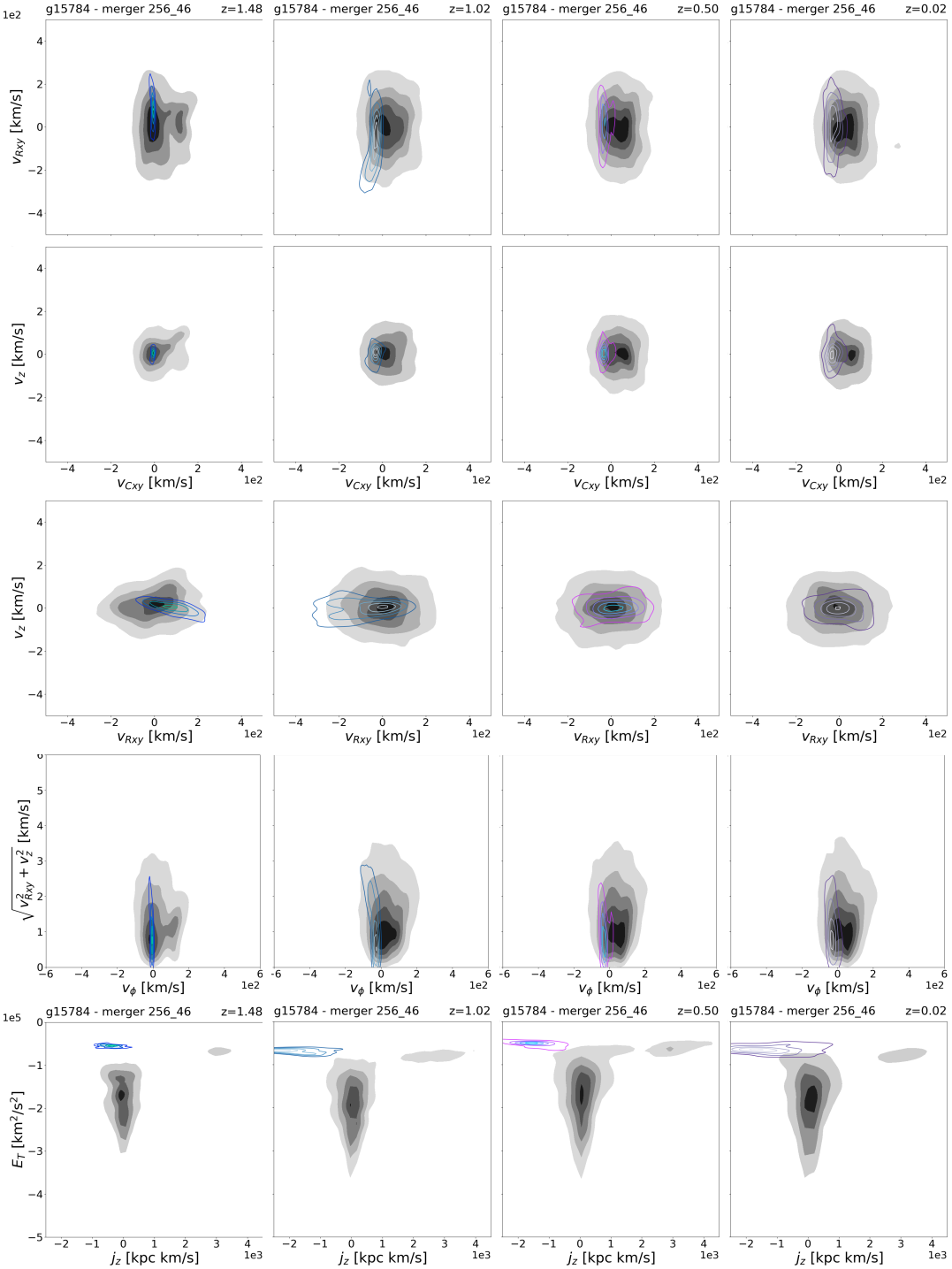

Figure 5.10: Temporal evolution of merger "256-46" (*Sequoia analogue*) in velocity and IoM spaces. Each panel represent a different redshift, namely: 1.48, 1.02, 0.05, and 0.02.

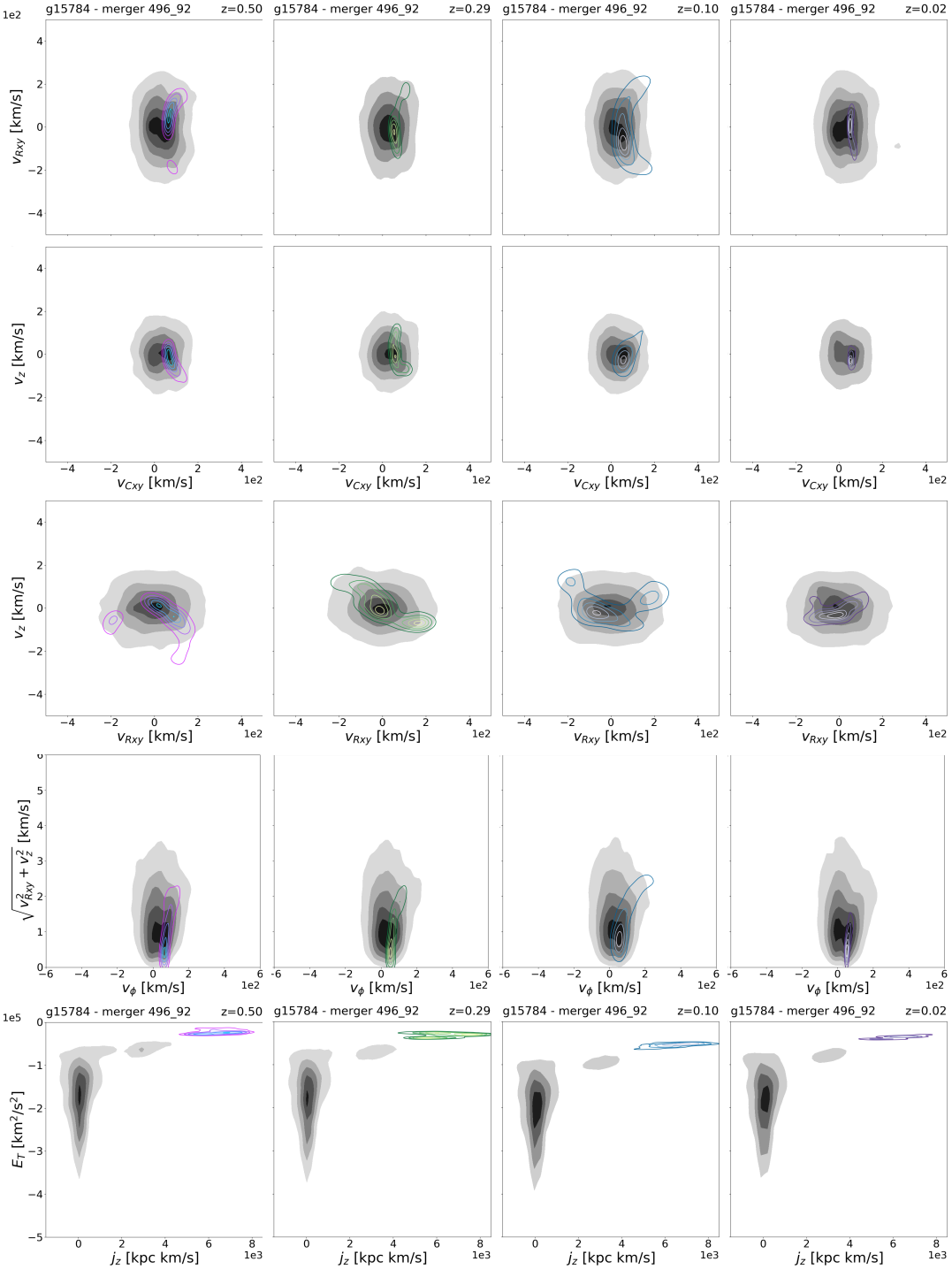

Figure 5.11: Temporal evolution of merger "496-92" (*Sagittarius analogue*) in velocity and IoM spaces. Each panel represent a different redshift, namely: 0.50, 0.29, 0.10, and 0.02.

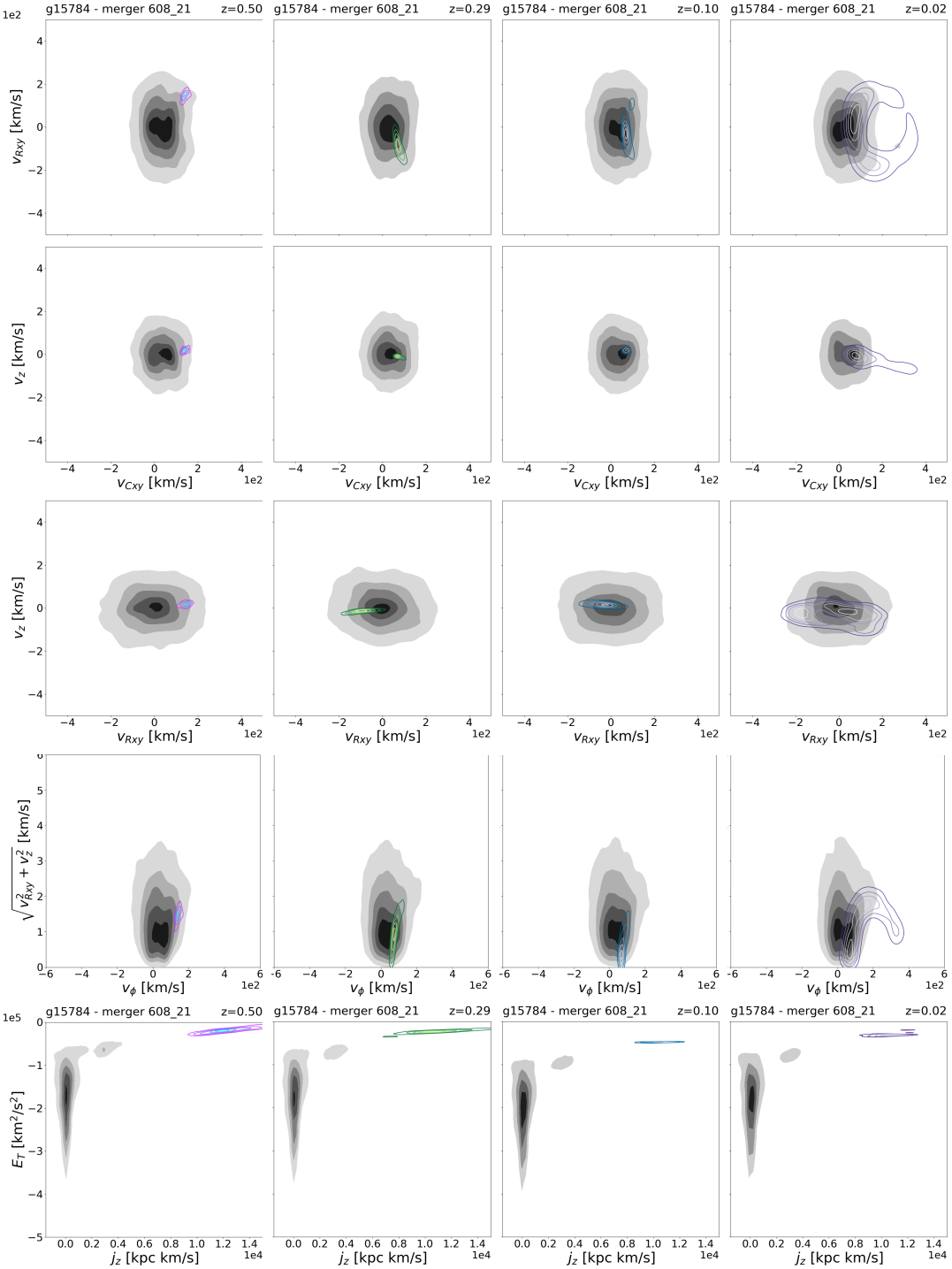

Figure 5.12: Temporal evolution of merger "608-21" in velocity and IoM spaces. Each panel represent a different redshift, namely: 0.50, 0.29, 0.10, and 0.02.

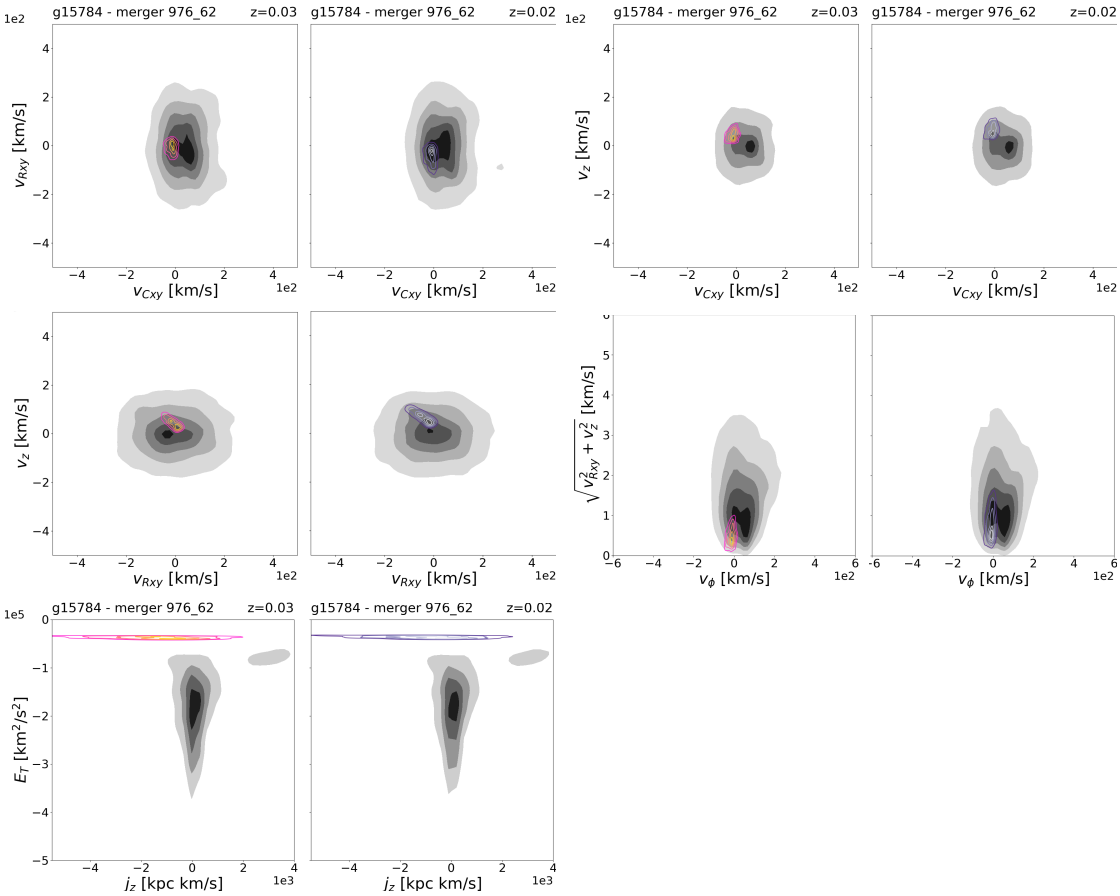

Figure 5.13: Temporal evolution of merger "976-62" in velocity and IoM spaces. Each panel represent a different redshift, namely: 0.03, and 0.02.

Chapter 6

Conclusion and Outlook

The formation and evolution of galaxies is an active field of study nowadays. Diverse studies, using data from both numerical simulations and observational missions, are currently being carried out aiming to disentangle the past of the Milky Way and the outcomes of its path of evolution. Although there has been an enormous amount of new information given by these studies, there is still a long way to go in order to discover the whole scenario that has made possible the creation our galaxy and the Universe beyond.

In this project, we have used a cosmological simulation of a Milky Way analogue from the MaGICC program to characterise a selection of mergers in terms of stellar mass, accretion redshifts and kinematical properties. In particular, we have taken analogues of Gaia-Enceladus and the Sagittarius dwarf galaxy, along with 6 other objects with no related observational structures. However, it is found a possible analogue of the Sequoia structure in the sample, according to its values of total energy and of the z-component of the angular momentum.

We analysed the phase space distributions of these mergers in several timesteps of their evolution within the central galaxy, and compared the main features between those mergers with early times of accretion and those with later times of infall. The main differences noticed here are the generally more random motion of early mergers, against the predominant rotation (sometimes retrograde) of late mergers. Also, earlier mergers tend to have lower total energies at z = 0.02, with the mean usually below -2.0×10^5 km^2/s^2, being strongly bound to the galaxy. Nevertheless, we find two exceptions that have higher average total energies, between -2.0×10^5 and -1.0×10^5 km^2/s^2. On the other hand, late mergers are located at higher energies, $E_T > -1.0 \times 10^5$ km^2/s^2, meaning that they are weakly bound to the system. Moreover, early mergers are found to be more phase-mixed at the present day, whilst later mergers still show defined individual structures, due to their shorter evolution as part of the galaxy. We studied the effects of a major merger analogue to Gaia-Enceladus on other accreted stellar objects. Its infall seems to cause an increase in the dispersion of the vertical velocity component of previous mergers, which recalls to the thick disk heating for in-situ stars due to the same merger event.

It has also been possible to explore the contribution of these mergers to the inner spheroid of the spiral galaxy and their surface density profiles at the present day. The results indicate that early mergers are mainly concentrated in the innermost region of the bulge, but contribute more to the outer part. On the contrary, the presence of late mergers is almost zero in this zone and they appear more scattered throughout the galaxy. We observe that the largest contribution

to both regions stems from the GE merger analogue, although only $\sim 14\%$ of its progenitor is found there. Accreted stars seem to be only a small part of the total stellar population within the bulge, being this region dominated by in-situ stars instead. Besides, the majority of ex-situ stars are placed in the outer stellar regions (>70%).

In addition, we analyse the temporal variation of the radial distance of the mergers together with the star formation history of each one of them, fulfilling the main aims of this work. Mergers with early accretions fall directly and from closer distances to the central system, while the rest originate at larger distances and display several apocentric and pericentric passages before their accretion. We find that the early mergers of the sample suffer enhancements of star formation before their infall, probably because of a compression of the gas during the process of accretion. Later mergers generally have longer SFH, but show a progressive decay in the SFR from 2-3 Gyrs of age of the Universe. These results imply that the population of stars from early mergers is older than the population from later mergers.

One possible path to continue with the analysis given in this report would be selecting a wider sample of mergers to be able to explore their properties by statistical means. Furthermore, this could lead to the uncovering of more analogues to real structures of the Milky Way. The characterisation of these analogues, along with the study of their evolution (before and after their accretion), would help to make additional comparisons with the results from observational research and provide extra information about these objects, such as trajectories (e.g. inclination and eccentricity of stars), mass ratios, impact on the galaxy, etc. In addition, an in-depth study on the rotation of late mergers and the phenomena causing it would be needed to better understand the kinematics of these bodies. A similar analysis than the one done in this work in phase space, but limited within the solar neighbourhood, would also offer important data to define these structures and detect the differences arisen from considering the whole galaxy against the region within observational reach nowadays. To take a step further, it would be appealing to examine the metallicities of mergers and the variation of this magnitude with time to better describe their influence in the system. Additionally, the analysis on the gas content of the satellite galaxies would offer further details in their star formation process while circling around the galaxy and being accreted into the main system. Lastly, the analysis and comparison between these results and those obtained with other Milky Way-like galaxies (especially those with a Gaia-Enceladus analogue) developed by using different numerical simulations would lead to interesting results in order to verify the formation process of our galaxy, as well as to contribute with more statistical knowledge about its merger history.

Bibliography

Abraham, R. G., van den Bergh, S., Glazebrook, K., Ellis, R. S., Santiago, B. X., Surma, P., & Griffiths, R. E. (1996). *ApJS*, *107*, 1. https://doi.org/10.1086/192352

Bell, E. F., Zucker, D. B., Belokurov, V., Sharma, S., Johnston, K. V., Bullock, J. S., Hogg, D. W., Jahnke, K., de Jong, J. T. A., Beers, T. C., Evans, N. W., Grebel, E. K., Ivezić, Ž., Koposov, S. E., Rix, H.-W., Schneider, D. P., Steinmetz, M., & Zolotov, A. (2008). *ApJ*, *680*(1), 295–311. https://doi.org/10.1086/588032

Belokurov, V., Erkal, D., Evans, N. W., Koposov, S. E., & Deason, A. J. (2018). *MNRAS*, *478*(1), 611–619. https://doi.org/10.1093/mnras/sty982

Belokurov, V., Zucker, D. B., Evans, N. W., Gilmore, G., Vidrih, S., Bramich, D. M., Newberg, H. J., Wyse, R. F. G., Irwin, M. J., Fellhauer, M., Hewett, P. C., Walton, N. A., Wilkinson, M. I., Cole, N., Yanny, B., Rockosi, C. M., Beers, T. C., Bell, E. F., Brinkmann, J., ... Lupton, R. (2006). *ApJ*, *642*(2), L137–L140. https://doi.org/10.1086/504797

Belokurov, V., Sanders, J. L., Fattahi, A., Smith, M. C., Deason, A. J., Evans, N. W., & Grand, R. J. J. (2020). *MNRAS*, *494*(3), 3880–3898. https://doi.org/10.1093/mnras/staa876

Bland-Hawthorn, J., & Gerhard, O. (2016). *ARA&A*, *54*, 529–596. https://doi.org/10.1146/annurev-astro-081915-023441

Blumenthal, G. R., Faber, S. M., Primack, J. R., & Rees, M. J. (1984). *Nature*, *311*, 517–525. https://doi.org/10.1038/311517a0

Brook, C. B., Stinson, G., Gibson, B. K., Wadsley, J., & Quinn, T. (2012). *MNRAS*, *424*(2), 1275–1283. https://doi.org/10.1111/j.1365-2966.2012.21306.x

Brook, C. B., Kawata, D., Gibson, B. K., & Flynn, C. (2003). *ApJ*, *585*(2), L125–L129. https://doi.org/10.1086/374306

Brook, C. B., Kawata, D., Gibson, B. K., & Flynn, C. (2004). *MNRAS*, *349*(1), 52–56. https://doi.org/10.1111/j.1365-2966.2004.07464.x

Brook, C. B., Kawata, D., Gibson, B. K., Gallart, C., & Vicente, A. (2020). *MNRAS*, *495*(3), 2645–2651. https://doi.org/10.1093/mnras/staa992

Cautun, M., Deason, A. J., Frenk, C. S., & McAlpine, S. (2018). *MNRAS*, *483*(2), 2185–2196. https://doi.org/10.1093/mnras/sty3084

Chabrier, G. (2003). *PASP*, *115*(809), 763–795. https://doi.org/10.1086/376392

Chaplin, W. J., Serenelli, A. M., Miglio, A., Morel, T., Mackereth, J. T., Vincenzo, F., Kjeldsen, H., Basu, S., Ball, W. H., Stokholm, A., Verma, K., Mosumgaard, J. R., Silva Aguirre, V., Mazumdar, A., Ranadive, P., Antia, H. M., Lebreton, Y., Ong, J., Appourchaux, T., ... Yıldız, M. (2020). *Nature Astronomy*, *4*, 382–389. https://doi.org/10.1038/s41550-019-0975-9

Chiba, M., & Beers, T. C. (2000). *ApJ*, *119*(6), 2843–2865. https://doi.org/10.1086/301409

Conselice, C. J. (2014). *ARA&A*, *52*(1), 291–337. https://doi.org/10.1146/annurev-astro-081913-040037

Cooper, A. P., Cole, S., Frenk, C. S., White, S. D. M., Helly, J., Benson, A. J., De Lucia, G., Helmi, A., Jenkins, A., Navarro, J. F., Springel, V., & Wang, J. (2010). *MNRAS*, *406*(2), 744–766. https://doi.org/10.1111/j.1365-2966.2010.16740.x

Crain, R. A., Schaye, J., Bower, R. G., Furlong, M., Schaller, M., Theuns, T., Dalla Vecchia, C., Frenk, C. S., McCarthy, I. G., Helly, J. C., Jenkins, A., Rosas-Guevara, Y. M., White, S. D. M., & Trayford, J. W. (2015). *MNRAS*, *450*(2), 1937–1961. https://doi.org/10.1093/mnras/stv725

De Silva, G. M., Freeman, K. C., Bland-Hawthorn, J., Martell, S., de Boer, E. W., Asplund, M., Keller, S., Sharma, S., Zucker, D. B., Zwitter, T., Anguiano, B., Bacigalupo, C., Bayliss, D., Beavis, M. A., Bergemann, M., Campbell, S., Cannon, R., Carollo, D., Casagrande, L., ... Žerjal, M. (2015). *MNRAS*, *449*(3), 2604–2617. https://doi.org/10.1093/mnras/stv327

Di Cintio, A., Mostoghiu, R., Knebe, A., & Navarro, J. F. (2021). *MNRAS*, *506*(1), 531–545. https://doi.org/10.1093/mnras/stab1682

Di Matteo, P., Haywood, M., Lehnert, M. D., Katz, D., Khoperskov, S., Snaith, O. N., Gómez, A., & Robichon, N. (2019). *A&A*, *632*, A4. https://doi.org/10.1051/0004-6361/201834929

El-Badry, K., Bland-Hawthorn, J., Wetzel, A., Quataert, E., Weisz, D. R., Boylan-Kolchin, M., Hopkins, P. F., Faucher-Giguère, C.-A., Kereš, D., & Garrison-Kimmel, S. (2018). *MNRAS*, *480*(1), 652–668. https://doi.org/10.1093/mnras/sty1864

Ferland, G. J., Korista, K. T., Verner, D. A., Ferguson, J. W., Kingdon, J. B., & Verner, E. M. (1998). *PASP*, *110*(749), 761–778. https://doi.org/10.1086/316190

Frenk, C. S., White, S. D. M., Efstathiou, G., & Davis, M. (1985). *Nature*, *317*(6038), 595–597. https://doi.org/10.1038/317595a0

Gaia Collaboration, Brown, A. G. A., Vallenari, A., Prusti, T., de Bruijne, J. H. J., Babusiaux, C., Bailer-Jones, C. A. L., Biermann, M., Evans, D. W., Eyer, L., Jansen, F., Jordi, C., Klioner, S. A., Lammers, U., Lindegren, L., Luri, X., Mignard, F., Panem, C., Pourbaix, D., ... Zwitter, T. (2018). *A&A*, *616*, A1. https://doi.org/10.1051/0004-6361/201833051

Gallart, C., Bernard, E. J., Brook, C. B., Ruiz-Lara, T., Cassisi, S., Hill, V., & Monelli, M. (2019). *Nature Astronomy*, *3*, 932–939. https://doi.org/10.1038/s41550-019-0829-5

García Bethencourt, G. (2020). http://riull.ull.es/xmlui/handle/915/20694

Gibson, B. K., Pilkington, K., Brook, C. B., Stinson, G. S., & Bailin, J. (2013). *A&A*, *554*, A47. https://doi.org/10.1051/0004-6361/201321239

Gill, S. P. D., Knebe, A., & Gibson, B. K. (2004). *MNRAS*, *351*(2), 399–409. https://doi.org/10.1111/j.1365-2966.2004.07786.x

Gingold, R. A., & Monaghan, J. J. (1977). *MNRAS*, *181*(3), 375–389. https://doi.org/10.1093/mnras/181.3.375

Grand, R. J. J., Bustamante, S., Gómez, F. A., Kawata, D., Marinacci, F., Pakmor, R., Rix, H.-W., Simpson, C. M., Sparre, M., & Springel, V. (2017). *MNRAS*, *474*(3), 3629–3639. https://doi.org/10.1093/mnras/stx3025

Grand, R. J. J., Gómez, F. A., Marinacci, F., Pakmor, R., Springel, V., Campbell, D. J. R., Frenk, C. S., Jenkins, A., & White, S. D. M. (2017). *MNRAS*, *467*(1), 179–207. https://doi.org/10.1093/mnras/stx071

Guo, Q., White, S., Boylan-Kolchin, M., De Lucia, G., Kauffmann, G., Lemson, G., Li, C., Springel, V., & Weinmann, S. (2011). *MNRAS*, *413*(1), 101–131. https://doi.org/10.1111/j.1365-2966.2010.18114.x

Haardt, F., & Madau, P. (1996). *ApJ*, *461*, 20. https://doi.org/10.1086/177035

Helmi, A., & White, S. D. M. (1999). *MNRAS*, *307*(3), 495–517. https://doi.org/10.1046/j.1365-8711.1999.02616.x

Helmi, A. (2020). *ARA&A*, *58*(1), 205–256. https://doi.org/10.1146/annurev-astro-032620-021917

Helmi, A., Babusiaux, C., Koppelman, H. H., Massari, D., Veljanoski, J., & Brown, A. G. A. (2018). *Nature*, *563*(7729), 85–88. https://doi.org/10.1038/s41586-018-0625-x

Helmi, A., Cooper, A. P., White, S. D. M., Cole, S., Frenk, C. S., & Navarro, J. F. (2011). *ApJL*, *733*(1), Article L7, L7. https://doi.org/10.1088/2041-8205/733/1/L7

Helmi, A., & Tim de Zeeuw, P. (2000). *MNRAS*, *319*(3), 657–665. https://doi.org/10.1046/j.1365-8711.2000.03895.x

Helmi, A., Veljanoski, J., Breddels, M. A., Tian, H., & Sales, L. V. (2017). *A&A*, *598*, Article A58, A58. https://doi.org/10.1051/0004-6361/201629990

Helmi, A., White, S. D. M., de Zeeuw, P. T., & Zhao, H. (1999). *Nature*, *402*(6757), 53–55. https://doi.org/10.1038/46980

Helmi, A., White, S. D. M., & Springel, V. (2002). *Phys. Rev. D*, *66*, 063502. https://doi.org/10.1103/PhysRevD.66.063502

Ibata, R. A., Gilmore, G., & Irwin, M. J. (1994). *Nature*, *370*(6486), 194–196. https://doi.org/10.1038/370194a0

Ibata, R., Bellazzini, M., Thomas, G., Malhan, K., Martin, N., Famaey, B., & Siebert, A. (2020). *ApJL*, *891*(1), L19. https://doi.org/10.3847/2041-8213/ab77c7

Johnston, K. V. (1998). *ApJ*, *495*(1), 297–308. https://doi.org/10.1086/305273

Johnston, K. V., Hernquist, L., & Bolte, M. (1996). *ApJ*, *465*, 278. https://doi.org/10.1086/177418

Kennicutt, J., Robert C. (1998). *ApJ*, *498*(2), 541–552. https://doi.org/10.1086/305588

Knollmann, S. R., & Knebe, A. (2009). *ApJS*, *182*(2), 608–624. https://doi.org/10.1088/0067-0049/182/2/608

Koppelman, H., Helmi, A., & Veljanoski, J. (2018). *ApJL*, *860*(1), L11. https://doi.org/10.3847/2041-8213/aac882

Koppelman, H. H., Helmi, A., Massari, D., Price-Whelan, A. M., & Starkenburg, T. K. (2019). *A&A*, *631*, Article L9, L9. https://doi.org/10.1051/0004-6361/201936738

Kormendy, J. (2013). https://doi.org/10.48550/ARXIV.1311.2609

Kruijssen, J. M. D., Pfeffer, J. L., Chevance, M., Bonaca, A., Trujillo-Gomez, S., Bastian, N., Reina-Campos, M., Crain, R. A., & Hughes, M. E. (2020). *MNRAS*, *498*(2), 2472–2491. https://doi.org/10.1093/mnras/staa2452

Kunder, A., Kordopatis, G., Steinmetz, M., Zwitter, T., McMillan, P. J., Casagrande, L., Enke, H., Wojno, J., Valentini, M., Chiappini, C., Matijevič, G., Siviero, A., de Laverny, P., Recio-Blanco, A., Bijaoui, A., Wyse, R. F. G., Binney, J., Grebel, E. K., Helmi, A., ... Mosser, B. (2017). *ApJ*, *153*(2), 75. https://doi.org/10.3847/1538-3881/153/2/75

Mackereth, J. T., Schiavon, R. P., Pfeffer, J., Hayes, C. R., Bovy, J., Anguiano, B., Allende Prieto, C., Hasselquist, S., Holtzman, J., Johnson, J. A., Majewski, S. R., O'Connell, R., Shetrone, M., Tissera, P. B., & Fernández-Trincado, J. G. (2019). *MNRAS*, *482*(3), 3426–3442. https://doi.org/10.1093/mnras/sty2955

Majewski, S. R., Schiavon, R. P., Frinchaboy, P. M., Prieto, C. A., Barkhouser, R., Bizyaev, D., Blank, B., Brunner, S., Burton, A., Carrera, R., Chojnowski, S. D., Cunha, K., Epstein, C., Fitzgerald, G., Pérez, A. E. G., Hearty, F. R., Henderson, C., Holtzman, J. A., Johnson, J. A., ... Zamora, O. (2017). *ApJ*, *154*(3), 94. https://doi.org/10.3847/1538-3881/aa784d

Malhan, K., Ibata, R. A., Sharma, S., Famaey, B., Bellazzini, M., Carlberg, R. G., D'Souza, R., Yuan, Z., Martin, N. F., & Thomas, G. F. (2022). *ApJ*, *926*(2), 107. https://doi.org/10.3847/1538-4357/ac4d2a

Massari, D., Koppelman, H. H., & Helmi, A. (2019). *A&A*, *630*, L4. https://doi.org/10.1051/0004-6361/201936135

Matsuno, T., Aoki, W., & Suda, T. (2019). *ApJL*, *874*(2), L35. https://doi.org/10.3847/2041-8213/ab0ec0

Monaghan, J. J. (1992). *ARA&A*, *30*(1), 543–574. https://doi.org/10.1146/annurev.aa.30.090192.002551

Myeong, G. C., Vasiliev, E., Iorio, G., Evans, N. W., & Belokurov, V. (2019). *MNRAS*, *488*(1), 1235–1247. https://doi.org/10.1093/mnras/stz1770

Peebles, P. J. E. (1998). https://doi.org/10.48550/ARXIV.ASTRO-PH/9806201

Penzias, A. A., & Wilson, R. W. (1965). *ApJ*, *142*, 419–421. https://doi.org/10.1086/148307

Planck Collaboration, Aghanim, N., Akrami, Y., Ashdown, M., Aumont, J., Baccigalupi, C., Ballardini, M., Banday, A. J., Barreiro, R. B., Bartolo, N., Basak, S., Battye, R., Benabed, K., Bernard, J. .-., Bersanelli, M., Bielewicz, P., Bock, J. J., Bond, J. R., Borrill, J., ... Zonca, A. (2020). *A&A*, *641*, Article A6, A6. https://doi.org/10.1051/0004-6361/201833910

Pontzen, A., Roškar, R., Stinson, G. S., Woods, R., Reed, D. M., Coles, J., & Quinn, T. R. (2013).

Robertson, B. E., & Kravtsov, A. V. (2008). *ApJ*, *680*(2), 1083–1111. https://doi.org/10.1086/587796

Ruiz-Lara, T., Gallart, C., Bernard, E. J., & Cassisi, S. (2020). *Nature Astronomy*, *4*, 965–973. https://doi.org/10.1038/s41550-020-1097-0

Ruiz-Lara, T., Matsuno, T., Lövdal, S. S., Helmi, A., Dodd, E., & Koppelman, H. H. (2022). *arXiv e-prints*. https://doi.org/10.48550/ARXIV.2201.02405

Schaye, J., Crain, R. A., Bower, R. G., Furlong, M., Schaller, M., Theuns, T., Dalla Vecchia, C., Frenk, C. S., McCarthy, I. G., Helly, J. C., Jenkins, A., Rosas-Guevara, Y. M., White, S. D. M., Baes, M.,

Booth, C. M., Camps, P., Navarro, J. F., Qu, Y., Rahmati, A., ... Trayford, J. (2015). *MNRAS*, *446*(1), 521–554. https://doi.org/10.1093/mnras/stu2058

Schmidt, M. (1959). *ApJ*, *129*, 243. https://doi.org/10.1086/146614

Shen, S., Wadsley, J., & Stinson, G. (2010). *MNRAS*, *407*(3), 1581–1596. https://doi.org/10.1111/j.1365-2966.2010.17047.x

Spergel, D. N., Bean, R., Doré, O., Nolta, M. R., Bennett, C. L., Dunkley, J., Hinshaw, G., Jarosik, N., Komatsu, E., Page, L., Peiris, H. V., Verde, L., Halpern, M., Hill, R. S., Kogut, A., Limon, M., Meyer, S. S., Odegard, N., Tucker, G. S., ... Wright, E. L. (2007). *ApJL*, *170*(2), 377–408. https://doi.org/10.1086/513700

Springel, V., White, S. D. M., Jenkins, A., Frenk, C. S., Yoshida, N., Gao, L., Navarro, J., Thacker, R., Croton, D., Helly, J., Peacock, J. A., Cole, S., Thomas, P., Couchman, H., Evrard, A., Colberg, J., & Pearce, F. (2005). *Nature*, *435*(7042), 629–636. https://doi.org/10.1038/nature03597

Starkenburg, E., Oman, K. A., Navarro, J. F., Crain, R. A., Fattahi, A., Frenk, C. S., Sawala, T., & Schaye, J. (2017). *MNRAS*, *465*(2), 2212–2224. https://doi.org/10.1093/mnras/stw2873

Stinson, G. S., Bailin, J., Couchman, H., Wadsley, J., Shen, S., Nickerson, S., Brook, C., & Quinn, T. (2010). *MNRAS*, *408*(2), 812–826. https://doi.org/10.1111/j.1365-2966.2010.17187.x

Stinson, G. S., Brook, C., Macciò, A. V., Wadsley, J., Quinn, T. R., & Couchman, H. M. P. (2012). *MNRAS*, *428*(1), 129–140. https://doi.org/10.1093/mnras/sts028

Stinson, G., Seth, A., Katz, N., Wadsley, J., Governato, F., & Quinn, T. (2006). *MNRAS*, *373*(3), 1074–1090. https://doi.org/10.1111/j.1365-2966.2006.11097.x

Tumlinson, J. (2009). *ApJ*, *708*(2), 1398–1418. https://doi.org/10.1088/0004-637x/708/2/1398

Vasiliev, E., & Belokurov, V. (2020). *MNRAS*, *497*(4), 4162–4182. https://doi.org/10.1093/mnras/staa2114

Villalobos, Á., & Helmi, A. (2008). *MNRAS*, *391*(4), 1806–1827. https://doi.org/10.1111/j.1365-2966.2008.13979.x

Villalobos, Á., & Helmi, A. (2009). *MNRAS*, *399*(1), 166–176. https://doi.org/10.1111/j.1365-2966.2009.15085.x

Vincenzo, F., Spitoni, E., Calura, F., Matteucci, F., Silva Aguirre, V., Miglio, A., & Cescutti, G. (2019). *MNRAS*, *487*(1), L47–L52. https://doi.org/10.1093/mnrasl/slz070

Wadsley, J. W., Veeravalli, G., & Couchman, H. M. P. (2008). *MNRAS*, *387*(1), 427–438. https://doi.org/10.1111/j.1365-2966.2008.13260.x

Wadsley, J., Stadel, J., & Quinn, T. (2004). *New Astronomy*, *9*(2), 137–158. https://doi.org/https://doi.org/10.1016/j.newast.2003.08.004

Walker, A. P., Gibson, B. K., Pilkington, K., Brook, C. B., Dutta, P., Stanimirović, S., Stinson, G. S., & Bailin, J. (2014). *MNRAS*, *441*(1), 525–531. https://doi.org/10.1093/mnras/stu419

Wang, L., Dutton, A. A., Stinson, G. S., Macciò, A. V., Penzo, C., Kang, X., Keller, B. W., & Wadsley, J. (2015). *MNRAS*, *454*(1), 83–94. https://doi.org/10.1093/mnras/stv1937

Waskom, M. L. (2021). *JOSS*, *6*(60), 3021. https://doi.org/10.21105/joss.03021

Zolotov, A., Willman, B., Brooks, A. M., Governato, F., Brook, C. B., Hogg, D. W., Quinn, T., & Stinson, G. (2009). *702*(2), 1058–1067. https://doi.org/10.1088/0004-637x/702/2/1058

Appendix A

Kernel Density Estimate plot

In this appendix, it is explained the method that have been applied to visualise the results in both, the velocity and Integrals of Motion spaces. This method is latter compared to the results that an ordinary two-dimensional histogram would offer.

To plot the stellar distributions of the sample of mergers we have used a function called `kdeplot`, from the Seaborn[1] (Waskom, 2021) module for Python. The name of this function refers to a "Kernel Density Estimation (KDE) Plot", that provides a visualisation with contours of the density distribution of particular bivariate (or univariate) dataset. It is analogous to an histogram, however, the KDE smooths the data using a Gaussian Kernel or filter to produce a more continuous set of lines than in histograms. Therefore, from a certain distribution of values, we obtain concentric contours that depict iso-proportions of density, i.e. the number of data points with the same or similar values per pixel.

The values associated to the contours are those of a normalised density. That is to say, the number of particles residing in each pixel of the grid (defined by the data) divided by the total number of particles. In this way, the sum of all density values multiplied by the pixel size is equal to the unity. The physical units of the density is $km^{-2}\ s^2$ for the diagrams in velocity space, and $kpc^{-1}\ km^{-3}\ s^3$ for the space defined by the total energy and the angular momentum. Nonetheless, the values of the contours are not exactly the same than those from a normal histogram, due to the usage of the Gaussian Kernel, that smooths the data. Additionally, the values of the contours obtained for an histogram rely on the number of bins chosen to represent the data, while the results of the KDE method depend on the gridsize. Analogously to an histogram, the contours are represented only from a certain density threshold. This means that those regions with lowest density of particles do not have any contour associated (see section A.0.1 for more details).

A.0.1 Comparison with a two-dimensional histogram

To understand how the KDE works in further detail, in this subsection we compare the results given by the KDE plot and those given by a two-dimensional histogram. The KDE plot is simply obtained through the `kdeplot` function from the two variables of study and, for this example, its contours have been derived from an equally-spaced array of 6 values. Besides, in this case, its limits have been set to coincide or be as close as possible to those resulting from the histogram

[1] https://seaborn.pydata.org/index.html

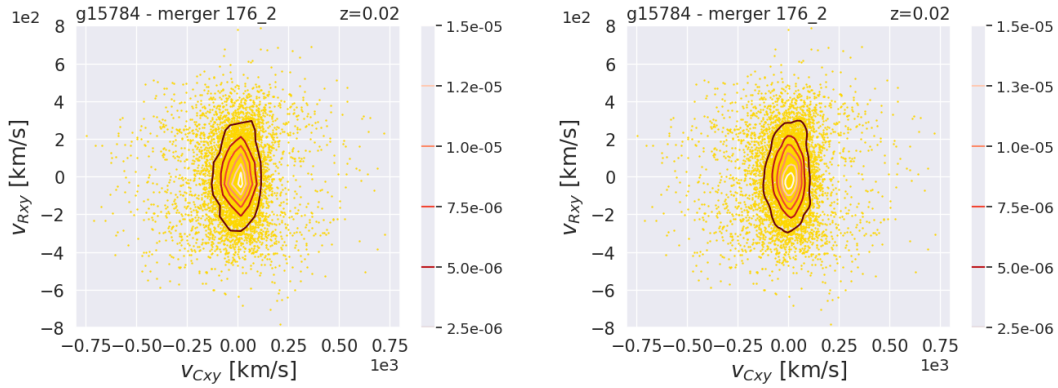

Figure A.1: Comparison between 2-d histogram (left) and KDE plot (right) for merger "176-2" at z = 0.02, in the space defined by v_{Cxy} and v_{Rxy}. The colorbars on the right of each panel show the values of each contour, that represent normalised iso-proportions of density of datapoints.

to be able to better compare both plots. On the other hand, to produce the histogram in two dimensions, we calculate the area of the pixels from the edges of the first and second bins, in both directions. In this way, we can compute the array of densities as the quotient of the number of particles in each cell and the area of the pixels. Then, this ratio is normalised by the total number of particles in the dataset, so the that integral density in the total area is equal to one. Finally, the coordinates associated to the grid cells are obtained as the middle point of each bin.

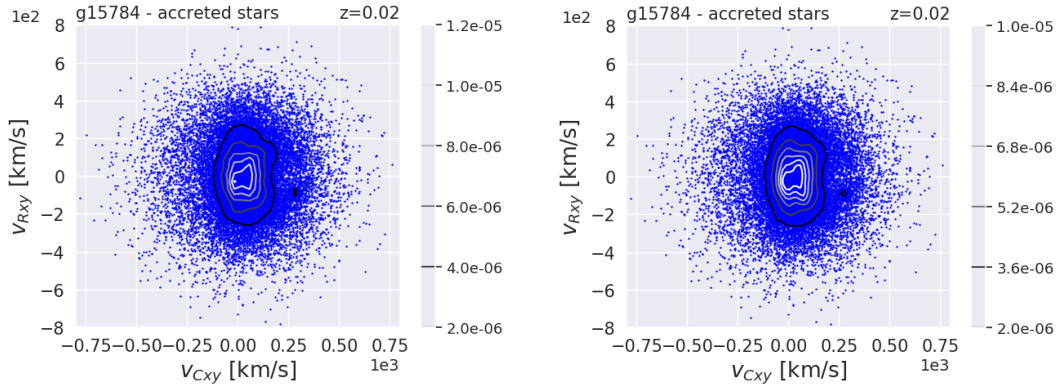

Figure A.2: Comparison between 2-d histogram (left) and KDE plot (right) for all accreted stars at z = 0.02, in the space defined by v_{Cxy} and v_{Rxy}. The colorbars on the right of each panel show the values of each contour, that represent normalised iso-proportions of density of datapoints.

As an example to visualise both methods, we have made two plots in the space defined by the azimuthal velocity, v_{Cxy}, and the radial velocity, v_{Rxy}, for two different distributions at redshift zero. These distributions are drawn from the "176-2" merger, with 7781 particles, and all the accreted stars, with a total number of 27409 particles. The plots are shown in figures A.1 and A.2, where the first panels represent the 2-d histogram and the second panels correspond to the KDE plot. The distribution of merger "176-2" can be seen in figure A.1 coloured in gold yellow

dots, where the red contours represent the values of density resulting from the aforementioned methods. The distribution corresponding to the accreted stars is presented in figure A.2 coloured in blue, where the density values are presented in grey contours. For the smaller distribution, it has been used a number of 42 bins on each side to construct the histogram, i.e. 1764 cells. For the larger distribution, this number has been of 28 bins on each side, this is 784 cells.

As we can see in the colorbars, the density values of both methods agree with each other for the two datasets, being more similar in the first case, for the individual merger. In figure A.1, outside of the contour associated to the lower limit (the outermost contour), the density of datapoints is smaller than 2.5×10^{-6} km^{-2} s^2, while inside of the central contour, the density is higher than 1.5×10^{-5} km^{-2} s^2. The same reasoning is applied for the distribution of all accreted stars, in figure A.2. On the other hand, the histogram contours also maintain a similar shape in both distributions with respect to the KDE plot, although this also depends on the number of cells employed to build the histogram.

For all of our final plots, we have set a number of 5 contours to represent the different distributions, and the density regions are automatically calculated through the `kdeplot` function from this number of contours. Additionally, colorbars are not displayed in the results, in order to centre attention in a more qualitative point of view with respect to the density, and focus on the examination of the kinematics of the accreted stars.